remote sensing

MDPI

Article

A Combination of Spatial Domain Filters to Detect Surface Ocean Current from Multi-Sensor Remote Sensing Data

Mohammed Abdul Athick AS [1,2,3] and Shih-Yu Lee [3,*]

[1] Taiwan International Graduate Program (TIGP), Earth System Science (ESS), Academia Sinica, Taipei 11529, Taiwan; as0191512@gate.sinica.edu.tw
[2] College of Earth Sciences, National Central University, Taoyuan 32001, Taiwan
[3] Research Center for Environmental Changes, Academia Sinica, Taipei 11529, Taiwan
* Correspondence: shihyu@gate.sinica.edu.tw

Abstract: This research investigates the applicability of combining spatial filter's algorithm to extract surface ocean current. Accordingly, the raster filters were tested on 80–13,505 daily images to detect Kuroshio Current (KC) on weekly, seasonal, and climatological scales. The selected raster filters are convolution, Laplacian, north gradient, sharpening, min/max, histogram equalization, standard deviation, and natural break. In addition, conventional data set of sea surface currents, sea surface temperature (SST), sea surface height (SSH), and non-conventional data such as total heat flux, surface density (SSD), and salinity (SSS) were employed. Moreover, controversial data on ocean color are included because very few studies revealed that chlorophyll-α is a proxy to SST in the summer to extract KC. Interestingly, the performance of filters is uniform and thriving for seasonal and on a climatological scale only by combining the algorithms. In contrast, the typical scenario of identifying Kuroshio signatures using an individual filter and by designating a value spectrum is inapplicable for specific seasons and data set. Furthermore, the KC's centerlines computed from SST, SSH, total heat flux, SSS, SSD, and chlorophyll-α correlate with sea surface currents. Deviations are observed in the various segments of Kuroshio's centerline extracted from heat flux, chlorophyll-α, and SSS flowing across Tokara Strait from northeast Taiwan to the south of Japan.

Keywords: spatial filters; data classification; Kuroshio detection; satellite remote sensing; oceanographic parameters; Argo drifter data

Citation: AS, M.A.A.; Lee, S.-Y. A Combination of Spatial Domain Filters to Detect Surface Ocean Current from Multi-Sensor Remote Sensing Data. *Remote Sens.* **2022**, *14*, 332. https://doi.org/10.3390/rs14020332

Academic Editors: Daniel F. Carlson and Yukiharu Hisaki

Received: 18 November 2021
Accepted: 5 January 2022
Published: 11 January 2022

1. Introduction

The recent advancements in satellite sensors and their algorithms have archived coherent, reliable, and high-resolution global oceanographic data for many decades. Moreover, satellite oceanography offers more extended practicality, possibilities, area averaging, repeated synoptic temporal observations, and prediction of KC from the same angle than just by using in-situ data [1,2].

Furthermore, the characteristics of Kuroshio water differ from those of its surroundings, and it forms a clear distinguished front of biophysical parameters such as SST, SSS, and chlorophyll-α [3,4]. As warm and saline water is brought into the study region (Figure 1) from the tropical pacific ocean, the SST and SSS of Kuroshio are higher than their surrounding waters. As a result, precise temperature and salinity boundaries formed at the north and western edges of the Kuroshio axis [5]. Therefore, satellite-based remote sensing from various sensors provides valuable knowledge for current ocean investigations.

AVHRR (Advanced Very High-Resolution Radiometer) and MODIS (Moderate Resolution Imaging Spectroradiometer) data help in detecting and monitoring the path, higher core temperature, and eddies of Luzon Strait in Kuroshio region, eastern coast of Japan, and the East China Sea [6–9]. However, studies conducted on the seas of East China, Huanghai, Bohai [10], and on the northeast continental shelf of the United States found that, during summer, the front thermal signatures fade and eventually disappear due to the uniform heat of the ocean surface [11].

It is noteworthy that the missing signature of the feature can be proxied from ocean color images. Under such circumstances, by employing eight-day composites of Sea-viewing Wide Field-of-view Sensor (SeaWiFS) ocean color images to map oceanic fronts using chlorophyll-α maxima and the intensity of spectral signature by chlorophyll-α in satellite images correlated with the volume of diatoms [12,13]. Within the nearshore region north of the Kuroshio and its southern part, the population of phytoplankton varies seasonally [14] and is comparatively reduced in the deep oceans throughout the year [15]. Still, chlorophyll-α is the largest in winter in the Kuroshio region and the other oceanic region [16]. However, variation of chlorophyll-α within the coastal zones and the offshore area along 135°25′E enhance in June, July, and August and is lesser during December, January, and February. Along with 137°E, it is more prominent in the fall season and very little in winter. Based on the above fact, numerous researchers from the ocean color research team of Japan have acknowledged that chlorophyll-α derived from various satellite images aids in mapping the Kuroshio extent during summer [17].

The diffused attenuation parameter (kd) from SeaWiFS Level-3 data mainly expressing turbidity both in the oceanic and coastal region at a wavelength of 490 nm used to gain knowledge about Kuroshio in the East China Sea, a pioneer in satellite-based oceanic studies [18]. Canadian, the United States, and Japanese research reported consistent SSD edifices associated with geostrophic currents. Moreover, the dominant nutrient density of zooplankton within these cyclonic circulations influences the path of KC. Higher density slows down the Kuroshio and leads to large meandering [19].

The counterpart of SST is SSS, a fundamental physical property of seawater, deriving thermohaline circulation. In addition, SSS is a prominent factors driving global climate change, and the interrelation between SST, chlorophyll-α, and SSS near the Antarctic ice was studied using satellite-derived data sets [20]. Regardless, few studies [21] used an unconventional strategy to detect surface front from multichannel satellites employing a neural network algorithm to differentiate Kuroshio from the South China Sea. As a result, they found that the salinity of Kuroshio water is very high compared to its surroundings.

Satellite altimetry is an additional dataset that provides knowledge about ocean circulation [22,23]. The main objective of SSH is to derive ocean currents [2,24,25] as the seawater naturally tends to move from increased sea level to the region of low sea level. Therefore, satellite altimetry likewise helps monitor the Kuroshio transport [26] and its variability of surface velocity [27].

Liu and Wu analyzed the role of heat release by evaporation in the Kuroshio region [28]. The localized air and sea interaction studies have primarily aimed at phase correlations among the latent (LHF), sensible heat flux (SHF), and the SST from monthly time scales. In addition, the thermodynamic property of seawater obtained by adding LHF and SHF represents total heat flux. Studies using heat flux confirm that the significant latent heat expands and forms a spatial boundary layer with distinct oceanic and meteorological attributes on either side of the Kuroshio extension [29–35].

However, directly measuring the total component of surface ocean currents from satellite investigations can only be possible by combining the observation from various sensors [36]. Therefore, the total combined surface current by summing the geostrophic and Ekman components from satellite altimetry and wind observation [37,38]. In addition, Agulhas current mapped using Globcurrent data products at 0 m to understand the atmospheric signature and its impact on local weather and climate [39]. Numerous scientific communities have investigated the fluctuations in the route, dimension, meandering, and velocity depending on the data from hydrographic in-situ observations, buoy (moored), and Lagrangian drifter [40–48]. Because of the extreme baroclinic structure, accelerated current, and influence of Kuroshio on the marine environment, operational agencies regularly monitor Kuroshio's information to aid navigation, fisheries, disaster prevention, and climate change studies [49]. The nutrient-depleted surface of KC is habitually quite turbulent and manifests substantial variations in its course and velocity [50–54].

The Argos satellite-tracking Lagrangian drifter has signified as a standard ocean current observational method for oceanographers to examine the surface velocity and its dispersion characteristics on the open ocean and marginal seas [55–58]. Nevertheless, the Argos Lagrangian drifter was confined to examine the surface velocity of the uppermost 15 m, and also Argos are unable to distinguish subsurface jet structures [59] in the southeast of Taiwan and Tokara Strait [60]. Therefore, multiple observational research has analyzed Argo Lagrangian drifters' fluctuations to study route, KC's extent, and velocity.

It is important to note that most studies recognized the Kuroshio front on standard dimensions (rectangular or square domain) based on their quantitative values from either physical, chemical, or biological parameters. For example, Takahashi and Kawamura [49] investigated the seasonal variation of Kuroshio through the two-dimensional histogram coupled with ranges of SST between 25–30 °C and chlorophyll-α about 0.03–0.4 mg m^{-3}. On the other hand, the objective method can spatially detect ocean fronts. The spatial mapping by an objective spatial filter method detects the sharp slope zones, also called edges formed by various open ocean physical processes (such as mixing, upwelling, and convergence). However, the conventional method using isotherms discussed above did not perform well during summer due to uniform surface heating; similarly, the extraction of features by only designating a range of values could not delineate the exact boundary of KC.

In order to delineate a feature from its surroundings, the effective and practical techniques are edge detection, cluster shadow method, and entropic approach [10,11,61–85]. Apart from the objective filters, the classification techniques, mainly natural-breaks Jenks optimization method and standard deviation, are widely used in remote sensing [86–88]. These classifications aid in spatially identifying the characteristics that are crucial or impossible to recognize precisely in multi-spectral remote sensing satellite data [89–91]. Likewise, the histogram and gradient filter are two widely accepted methods due to their fortitude, adequate universal validation, simplicity, and effortless implementation.

Accordingly, this study combines the previous findings in various aspects. First, we utilize all seven of the oceanographic satellite-driven parameters to test the efficiency of the spatial filter to distinguish the KC from its surrounding water masses. Furthermore, this research endeavors to answer the best combination of objective filter and spatial classification methods suitable for SST, SSH, total heat flux, SSS, SSD, chlorophyll-α, and sea surface currents—and the possibilities of mapping the entire extent of Kuroshio precisely with them. At the outset, weekly (typhoon Maria 3–12 July 2018 plus six days), seasonal (December 2015 to February 2016 during very strong El Nino), and monthly climatology means are computed between 20° to 40°N and 115° to 145°E for the whole duration of available satellite data. It is followed by detecting KC and its centerline by combining assorted raster stretching, spatial filters, and classification parametrization without any prerequisite gradient threshold for remote sensing images. Finally, to validate the distance and slope from SST, SSH, total heat flux, SSS, SSD, and chlorophyll-α were correlated with sea surface currents using slope and distance matrices. In addition, the Kuroshio centerline from all seven parameters was spatially overlaid on the Kuroshio extent mapped for January and July climatology from Lagrangian drifters [55–58,92] to visualize the proximity of KC derived from remote sensing parameters and Argo drifter data.

2. Data and Methods

2.1. Study Area

KC plays an essential part in the north Pacific circulation transporting seawater of volume equivalent to six thousand large rivers by advecting an appreciable amount of heat from tropic to northern mid-latitude. Therefore, any variation in KC's path can influence large/small scale climate changes. As one of the world's substantial elements among the northwest region of the subtropical Northern Pacific gyre, scientists and researchers from Hong Kong, United States, China, Singapore, Korea, Japan, Indonesia, Philippines, Thailand, Vietnam, and the Soviet Union, were associated in intercontinental research named "cooperative study of the

Kuroshio". Their investigation focused on understanding the changes in weather, climate, marine animals, and plants in response to Kuroshio condition [93].

Being the second most influential and swift current globally next to the Gulf Stream, KC actively engages as a carrier of meridional mass heat flux, momentum, and fresh water through the western boundary, approximately 3000 km [94]. The area of interest is between 20° to 40°N and 115° to 145°E, where Kuroshio flows from the Philippines on the north alongside the eastern Taiwan coastal regions towards the mid-continental shelf and break of the East China Sea. Then, Kuroshio crosses the Kyushu, including Tokara Strait, advancing northeast along Japan's south coast (Figure 1). Finally, it opens into the Pacific Ocean, where it comes under the influence of westerlies and turns eastward around 36°N flows across the ocean as the North Pacific Current [49,95–97].

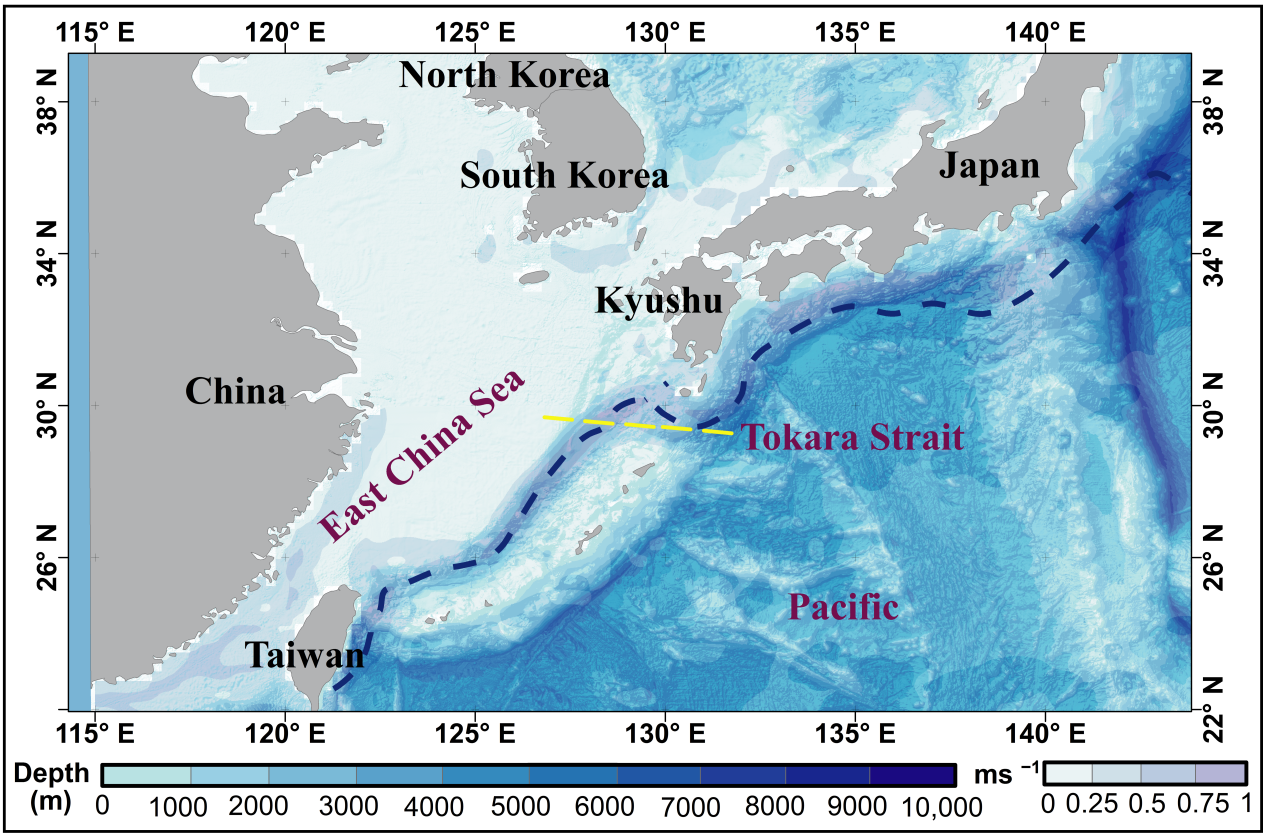

Figure 1. Base map of the study area illustrating bathymetry merged with sea surface current portraying Kuroshio's path in blue dashed line. The yellow dashed line denotes the position of Tokara strait where KC flows in 'U' pattern.

Three patterns of KC have been observed in the southern waters of Japan and categorized as: nearshore, offshore, and large/small meander [44–48]. Moreover, besides path variation, Sun [40] stated that KC also exhibits remarkable temperature and salinity changes. During winter, KC flows closer to the continental shelf of Taiwan and then slips notably apart through the summer. Nevertheless, KC is nearly parallel to the shoreline and illustrates no apparent periodical variations in the east of Taiwan [95,98]. The maximum KC velocity and width estimated at around 100 cm s^{-1}, and 170 km, concluded from ten-year shipboard acoustic Doppler current profilers [53].

2.2. Data

As discussed below, the daily data obtained from Argo Lagrangian drifters and various satellite missions are used for input and successive validation. Again, though, all datasets

provided on a global spatial resolution, only data covering the extent of the study area have been used.

2.2.1. Lagrangian Argo Drifter Data

Satellite tracked Argos Lagrangian drifters data from 1987 to 2019 provided by Atlantic oceanographic and meteorology (AOML). The composites of surface velocity (at sea surface) to validate the spatial proximity of the extracted Kuroshio path. These drifter data assembly centers, cataloged by AOML (www.aoml.noaa.gov/phod/argo, accessed on 10 June 2021), archive all ocean currents datasets using the network of drifters.

In this study, altogether, 585 Lagrangian drifter data obtained from satellite-tracked Argos were normalized to generate 0.25° latitude by 0.25° longitude grids. AOML uses quality management practices to revise these locations and temperatures to interpolate them on 6-hour intervals utilizing an optimum Kriging procedure, typically employed for 2D and 3D investigations. In addition, some drifters include bound sensors to measure salinity, pressure, wind speed, and direction.

Argo trajectory files include the information of Argos and the GPS location of drifters. These files likewise contain cycle timing details for the computation of velocity. The time data fields are from floats, estimations on float details in real-time, the satellites in real-time, or in delayed mode analyses. Nevertheless, the Argos drifters are limited to examining the surface velocity of the upper water column between 0 to 15 m [99].

2.2.2. Sea Surface Currents

Surface currents combined with regional and remote factors, including buoyancy fluxes, winds, waves, tides, and mixed layer depth tides. The 1/4° grid, daily geostrophic, and the Ekman currents from 1993 to 2018 are rendered as two different data products from GlobCurrent (version 3.0) (http://www.globcurrent.org/, accessed on 25 February 2021).

GlobCurrent data set is of global coverage portraying the geostrophic currents, the Ekman-component, tidal currents, and the Stokes drift at two different depths (valid at the surface (*hs*) and z = 15 m). At both depths, combined currents are computed as a sum of geostrophic and Ekman components as shown below:

$$\begin{aligned} Eastward_{combined}\ (z = hs) &= u_{geost} + u_{ek}\ (z = hs) \\ Northward_{combined}\ (z = hs) &= v_{geost} + v_{ek}\ (z = hs) \end{aligned} \quad (1)$$

where, $geost = geostrophic\ currents$ and $ek = Ekman\ Currents$. The geostrophic components of ocean current are from sea surface altimetry, anomalies, and contemporary mean dynamic topography [100], presenting an estimation of the time-averaged geostrophic current with a temporal and spatial resolution of 10 days and 100 to 150 km, respectively [101].

Ekman currents at the surface 0 and 15 m below are the modeling products of Ekman current. The parameters to run the model are trajectories of the drifting buoys (15 m) and the velocity determined from drifter floats. The fine-tuning of model parameters filters buoy data using 20 days band-pass filter. Eventually, the model is coupled with 3-hourly wind stress fields from ECMWF (European Centre for Medium-Range Weather Forecasts) with 80 km spatial resolution to provide the global current Ekman products. Although the sea surface currents are not the mere sum of various current components, the resultant $\sqrt{u^2 + v^2}$ of combined zonal ($u = Eastward_{combined}$) and meridional ($v = Northward_{combined}$) elements of GlobCurrent products at 0 m depth is utilized in this research [37].

2.2.3. SST

Optimum Interpolation SST (OISST version 2.1) is a high-resolution SST. We used the data set provided by NOAA/NESDIS (National Environmental Satellite, Data, and Information Service)/NCEI (National Centers for Environmental Information) with a temporal resolution of one day. Version 2.1 (https://www.ncei.noaa.gov/, accessed on 17 December 2020) is a blend of in-situ SST with AVHRR's SST. An infrared remote sensor of AVHRR provides the skin temperature of the sea surface water. The optimum interpolation

algorithm fills the spatial gaps to produce global coverage of SST. From January 2016 to the present time, modifications are:

1. In-Situ and drifter data transformed to traditional alphanumeric codes combined with the universal binary data format.
2. Obtaining SST also from Argo floats.
3. The satellite input is modernized to operational meteorological satellites A and B.
4. Revised ship-based buoy SST rectification method and sea-ice-concentration to SST.

However, OISSST version 2.0 incorporates only the data from ship and buoy for calibration. However, version 2.1 is obtained from 2.0 and includes ship, buoy, and Argo float observation from January 2016 to correct AVHRR's biases [102–105]. Therefore, this paper used 1982–2019 daily averaged version 2.1 data with a spatial resolution of $0.25^{\circ} \times 0.25^{\circ}$.

2.2.4. Heat Flux

The SeaFlux project examines and delivers a fine-resolution satellite data set of surface fluxes covering the global ocean (https://seaflux.org/, accessed on 19 November 2020). The sea flux products incorporate the following features:

1. A comprehensive data set from research vessels and drifters for validation.
2. Satellite and in-situ data are collected over a region of 200 km approximately around each point of situ.
3. Issued involving diurnal cycles are resolved using skin SST from refined high-resolution data.
4. Betterment of models to calculate bulk turbulent flux.
5. Surface air temperature and humidity retrieval from satellites.
6. Sea flux products are calibrated by applying the end products to physical phenomena, for instance, heat transport in the atmosphere and ocean.

Ocean heat flux products include SHF and LHF developed from multiple satellite missions such as SSMI (Special Sensor Microwave Imager), QuikSCAT (Quick Scatterometer), AVHRR, AMSR (Advanced Microwave Radiometer), and NCEP (National Centers for Environment Prediction) [106,107].

Sensible heat is related directly to change in temperature, whereas latent heat is with ocean surface evaporation [108]. The estimated accuracy of heat flux products is within 1 W m^{-2} correlated with flux measurements obtained over 120 buoys, indicating better computed satellite global flux observations. The study analyzed the combined $1/4^{\circ}$ equal angle grid of LHF and SHF energy products over 1988–2018 to map the Kuroshio.

2.2.5. Chlorophyll-α

The ocean color project has delivered global L3 (level 3) binned from multiple satellite sensors on daily and composites (5-day, 8-day, and monthly) time-series, emphasizing climatological studies. Version 4.2 contains sinusoidal projected chlorophyll-α (mg m^{-3}) in 4320 rows of latitude with 4 km vertical bins. The equal-area property of projection has maintained the varying latitude along with longitude. This ocean color data have an advanced algorithm to maintain only the bins with spatial information and omit the rest. Recently, the ocean color data are also in geographic projection (https://www.oceancolour.org/, accessed on 21 January 2021).

This study includes satellite-generated ocean color climate change initiative project data with 4 km spatial resolution between 1997 to 2019. The ocean color datasets are a blend of SeaWiFS, MERIS (Medium imaging spectrometer), MODIS-Aqua, and VIRS (Visible Infrared Imaging Radiometer) [109]. In addition, ocean color remote sensing offers chlorophyll-α digital signatures on time-series [110], representing phytoplankton bloom on comprehensive scales and assimilating using contemporary science with best-performing in-situ algorithms [111–113].

2.2.6. SSH

Satellite gridded altimetry measurements provide sea level anomaly. The mean decadal sea level is rising under the impact of global warming. Therefore, precise sea-level measurements are needed as this increasing sea level trend of an enormous magnitude would pose a danger to the coastal and low-lying regions. The height of the mean sea surface in a given time and space is well-defined as a sea surface anomaly. In this data set, sea level anomalies correspond between 1993–2012, employing advanced altimeters. The sea-level data set is furnished by a dedicated recording of the transition of sea level on a stable and homogenous scale. Moreover, practical data sets by merging the products from a constellation of remote sensing satellites provide global coverage.

SSH with a spatial resolution of $0.25^{\circ} \times 0.25^{\circ}$ above the geoid estimated between 1993 and 2019 from the sea level anomaly and mean dynamic topography together with geostrophic velocities used in this study (https://cds.climate.copernicus.eu/, accessed on 4 March 2021). The Sea Level dataset is a time series of daily gridded SSH and derived variables by merging two satellite altimetry measurements. The associate mission used for the altimetry processing is Topex/Poseidon between 1993 and 2002, Jason-1 between 2002 and 2008, OSTM/Jason-2 between 2008 and 2016, Jason-3 since 25 June 2016 [114]. Thus, this altimetry dataset is updated a year thrice with a delay of about six months. Moreover, these datasets are processed and validated to improve the firmness and precision of the sea level data to make them suitable for the climate and oceanographic applications.

2.2.7. SSS and SSD

Sea surface salinity and density play a significant part in the climate system and directly relate to the ocean dynamics with ocean-front distribution impacted by climate change [115,116]. Indeed, the global and regional water cycle has a consequential impact on salinity and, therefore, density.

The older version of the data set was merging the Argos and Conductivity Temperature Depth (CTD) measurements on a sparse global scale. The multivariate approaches blend in situ and satellite data to yield gap-free fields of SSS and SSD at considerably effective spatial and temporal resolution. Two prominent algorithms based on fusion techniques and optimal interpolation (OI) to linearly regress the satellite measurements (SSS and SSD). Four distinct compositions have been evaluated in the calibration of the algorithm to interpolate SSS and calculate the interrelated SSD [117–119].

In this study we used, gap-free Level-4 datasets ($1/4^{\circ} \times 1/4^{\circ}$ spatial resolution) of SSS and SSD covering the period from 1993 to 2019 obtained by an advanced multivariate optimal interpolation algorithm and satellite images on a regular grid from soil moisture ocean salinity (https://resources.marine.copernicus.eu/products, accessed on 18 March 2021).

2.3. Methods

Figure 2 illustrates the overall framework with the combination of filters and data classification followed in this research. In addition, this section presents the complex process with demanding significant image analysis steps includes image pre-processing [120,121], determining suitable filters, data algorithm, feature extraction, computation of midpoints with Kuroshio centerline, and accuracy assessment.

The estimated weekly, seasonal, and monthly climatologies are from the mean values of daily data used to map the association of mentioned parameters over Kuroshio in the study area. Our strategy to detect Kuroshio on a multi-variate proposition. First, the enhancement of spatial signatures at fronts associated with the feature is revealed in remote sensing images applying contextual filters and data classification methods. They eliminate noise but preserve the features, followed by edge detection to extract the features in satellite images that have been digitally analyzed with the combination of filters to preserve its features. The hierarchy and combination of filters and data processing algorithms are illustrated in Figure 2.

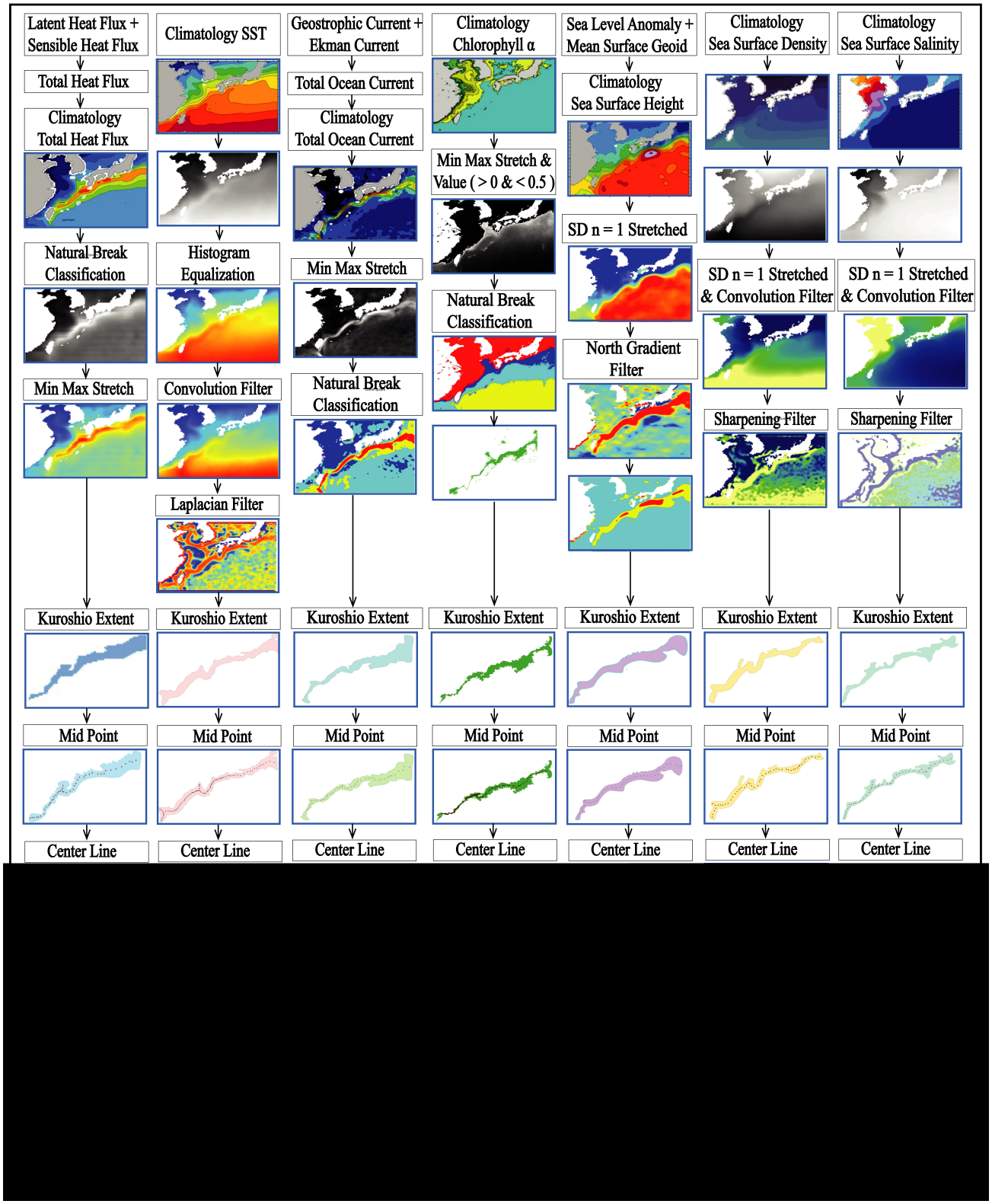

Figure 2. Methodology explaining the sequence of spatial filters and data analysis applied for each data set with their respective output.

2.3.1. Raster Filters

A convolution, Laplacian, and sharpening filters are fit to process the SST, SSD, and SSS climatological datasets in multiple combinations to achieve specific results to extract the Kuroshio centerline. These functions perform filtering on a pixel basis in a satellite

image to sharpen and detect edges of features within an image. The principal innovative approach of our filters is that it analyzes a small pixel window at a time within a more comprehensive large pixel window.

Convolution Filter

In our research, we applied a kernel of a convolution filter across all the pixels of an image. It is one of the most effective digital image analysis processes similar to a median filter that eliminates spurious data while preserving and enhancing the edges of the features. These are used in various front detection algorithms to pre-process in steps using a shifting 3×3 overlapping kernel [64]. Convolution filters operate by estimating the weighting pixel values of their neighbors. In oceanography, the first contextual filtering was used to classify the vertical profiles in addition to validating large-scale climatological datasets obtained from the Northern Pacific Ocean [73,122].

Laplacian Filter

A second derivative of the Laplacian filter [123] is further applied to enhance the Kuroshio regardless of edge direction. The Laplacian filter (L) passed over the climatological pixels (I) in both X and Y-axis is provided by:

$$L(X,Y) = \frac{\partial^2 I}{\partial X^2} + \frac{\partial^2 I}{\partial Y^2} \quad (2)$$

It is used on an image that has been improved, smoothed, and reduced sensitivity to noise. Indeed, a sliding 3×3-pixel window is emphasized peak values within an image applying a kernel with a high center value typically enclosed by negative odd kernel weights in the north-south and east-west pixel direction and zeroes at the corners of Kernel:

$$\nabla = \begin{bmatrix} 0 & 1 & 0 \\ 1 & -4 & 1 \\ 0 & 1 & 0 \end{bmatrix} \quad (3)$$

Sharpening Filter

We used a high-pass sharpening filter to strongly the relative variation in the values concerning its neighboring pixels. Our 5×5 high-pass filter determines the focal sum by spatial statistic by weighted pixel:

$$\nabla = \begin{bmatrix} -1 & -3 & -4 & -3 & -1 \\ -3 & 0 & 6 & 0 & -3 \\ -4 & 6 & 21 & 6 & -4 \\ -3 & 0 & 6 & 0 & -3 \\ -1 & 3 & -4 & -3 & -1 \end{bmatrix} \quad (4)$$

It reveals the boundaries between Kuroshio and its surrounding water masses by sharpening edges within features, especially in SSS and SSD datasets combined with other image processing algorithms. The high-pass filter is also known for enhancing edges. The logic behind this kernel is to automatically identify cells to use in the region and weigh them (i.e., multiply them) [124].

2.3.2. Gradient Computation

On a satellite image $f(x,y)$ at any coordinate of pixel (x,y), the gradient is a vector component:

$$\nabla f = \frac{G_x}{G_y} = \frac{\partial f / \partial x}{\partial f / \partial y} \quad (5)$$

During the gradient computation, the points of a vector are in the direction of the maximum rate of change of an image f at (x, y). In edge detection, a significant component is the magnitude of vector:

$$|\nabla f| = \sqrt{{G_x}^2 + {G_y}^2} \tag{6}$$

The maximum rate of increase in the gradient of $f(x, y)$ per unit distance in the direction of ∇f. The magnitude of a gradient vector is typically calculated using:

$$|\nabla f| = |G_x| + |G_y| \tag{7}$$

The direction of the gradient is given by:

$$\alpha(x, y) = tan^{-1} \frac{G_y}{G_x} \tag{8}$$

A nonlinear north gradient filter is used as one of the analysis methods to process SSH data. This gradient vector (G) on the y-axis is calculated by a 3×3, GY mask:

$$\nabla = \begin{bmatrix} -1 & -2 & -1 \\ 0 & 0 & 0 \\ 1 & 2 & 1 \end{bmatrix} \tag{9}$$

to enhance edges' visibility with 45° increments simply and effectively on satellite images and extensively used in various remote sensing applications. In addition, the Sobel operator is a derivative filter with a smoothing effect at each pixel containing approximations for direction with the most significant increase and how edges are oriented [125,126]; in our case, it is the y-axis:

$$\nabla = \begin{bmatrix} 1 & 2 & 1 \\ 0 & 0 & 0 \\ -1 & -2 & -1 \end{bmatrix} \tag{10}$$

2.3.3. Conditional Filtering

The detection of KC from chlorophyll-α was brought out in three stages. Firstly, as Takahashi et al. [49] proposed, the chlorophyll-α concentration in Kuroshio depends on the volume of various phytoplankton species. Moreover, they vary seasonally among open ocean, coastal regions, north and south of Kuroshio waters. Therefore, based on various iterations, Liu and Hou [18] used contour ranges of chlorophyll-α between 0.02 to 0.4 mg m^{-3} to show Kuroshio fronts between the water masses. Hence, in our study, we improvised the range of chlorophyll-α as a conditional filter to suit seasonal and climatological data:

$$0 < Chlorophyll\text{-}\alpha < 0.5 \text{ mg } m^{-3} \tag{11}$$

Secondly, we tested the values using a conditional filter to extract the pixels within the threshold values and mask the remaining to extract the extent of Kuroshio. The resultant image retains chlorophyll-α between 0 to 0.5 mg m^{-3}. When this image is viewed, the minimum brightness value of 0 to 0 mg m^{-3} and maximum of 255 to 0.5 mg m^{-3} are not depicted without enhancement. Therefore, applying a minimum-maximum linear contrast stretch [127,128]:

$$g(x, y) = \frac{f(x, y) - min}{max - min} * N \tag{12}$$

where,

$g(x, y)$ = Enhanced output image.
$f(x, y)$ = Input images after applying improvised range of chlorophyll-α.
min,max = Minimum and maximum intensity values of input image.

N = Total number of intensity values assigned to a pixel.

Finally, using Jenks natural breaks classification, the enhanced image was stratified by rationing values to a disseminated number of classes intending to minimize variances within classes simultaneously maximizing among class means [129]. The summary of filters used to extract the extent of KC from the selected seven satellite-based oceanographic parameters (Table 1) and the sequence in which they were applied (Figure 2).

Table 1. Overview of filters used for each parameter to delineate the KC.

Candidates	Heat Flux	SST	Sea Surfac Current	Chlorophyll-α	SSH	SSD	SSS
Natural Break Classification	✓		✓	✓			
Min-Max Stretch	✓		✓	✓			
Histogram Equalization		✓					
Convolution Filter		✓				✓	✓
Laplacian Filter		✓					
Conditional Filter				✓			
Standard Deviation Stretch_{n = 1}					✓	✓	✓
Sharpening Filter						✓	✓
North Gradient Filter					✓		

2.3.4. Classification Method to Represent Kuroshio

In multi-spectral remote sensing satellite data, the spectral classification methods aid with extracting quite complicated and hidden features [86–88]. The classification method used varies depending on the nature of the data. We employed natural break classification (Heat Flux and chlorophyll-α), minimum-maximum stretch (Heat Flux, sea surface current and chlorophyll-α), histogram equalized method (SST), and standard deviation (n = 1) (Argo drifter data, SSH, SSS, and SSD).

We also determined the number of classes so that, in such a way, the distribution-characteristic of original data does not change and can be expressed faithfully as methods suggested by Osaragi [91]. Natural Breaks classification distinguishes the breakpoints by scanning for groups and patterns integrated within the data. It is the most famous method used in spatial analysis to minimize variation within the data class.

The minimum-maximum, histogram equalized, and standard deviation stretches functions are applied to radiometric enhancing the satellite image by adjusting properties such as brightness, contrast, and gamma so that the eye can easily perceive Kuroshio. The minimum-maximum is a linear contrast stretch in which the initial minimum and maximum values of the original data are assigned to 0 and 255 on the computer screen. In some data such as SSH, SSS, and SSD, the majority of the pixel befall within a higher and lower limit. Therefore, we trimmed off the extreme values. It is done statistically by defining a linear standard deviation stretch applied between the values outlined by the standard deviation (n = 1) condition.

Similarly, histogram equalized is also a contrast stretch function to display more frequency values. Thus, it details the areas with the most significant frequency of pixel values. As a result, the SST pixels in Kuroshio are better enhanced than those in the original histogram, wherever values occur less frequently.

2.3.5. Feature Extraction

After stratifying the dataset by employing the hierarchy of coupled digital analysis techniques illustrated in Figure 2, the Kuroshio is visible on the satellite images. Then, to isolate the feature from its surroundings, the homogeneous cluster of pixels within the Kuroshio region are identified, eliminating the insignificant sub-pixel elements and after determining the Kuroshio region by feature extraction, followed by delineating the cluster of homogenous pixels by image segmentation.

The resultant Kuroshio extent by boundary extraction (image segmentation) is a vector format. At this point, by analyzing the boundaries of Kuroshio extent and they appear to be "step-like" as they follow a definite contour of pixels. To represent a more realistic

appearance of the features, 'steps' are softened by running a smoothing filter over the edges carefully without distorting the edges and causing a shift in latitude and longitude coordinates. Ultimately, calculating the midpoint between the similar top and bottom X coordinates with varying Y-coordinates throughout the Kuroshio polygon boundary layer length yields the vertex of centerline. Finally, connecting vertices obtained inside the polygon represent Kuroshio's centerline.

2.3.6. Correlation and Proximity Analysis

A correlation analysis was carried to understand the strength of linear relationship between two quantitative variables of the Kuroshio centerline obtained from the seven oceanographic parameters employed in this study. As the centerline is a linear feature, it attributes the only length. Therefore, to get more meaningful quantitative fields, all the centerlines must be brought to an equal distance, then calculate the number of pixels covered by each centerline via dividing the shape length and pixel size. The resultant is x and y coordinates of pixels in the same column varying concerning row as shown in Figure 3a,b. Finally, calculate quantitative fields from the origin using consequent coordinates, slope, and distance. Furthermore, the slope correlation matrix and distance correlation matrix demonstrate the linear relationship among various parameters.

Finally, the Kuroshio from SST, SSH, total heat flux, SSS, SSD, and chlorophyll-α is validated with Kuroshio from sea surface current as a reference using standard deviation and correlation from slope and distance using Taylor's plot. In addition to the correlation matrix and Taylor's plot, Kuroshio extent mapped from Lagrangian Argo drifters. Lastly, to examine proximity, all seven oceanographic parameters are overlaid on the results of drifter data.

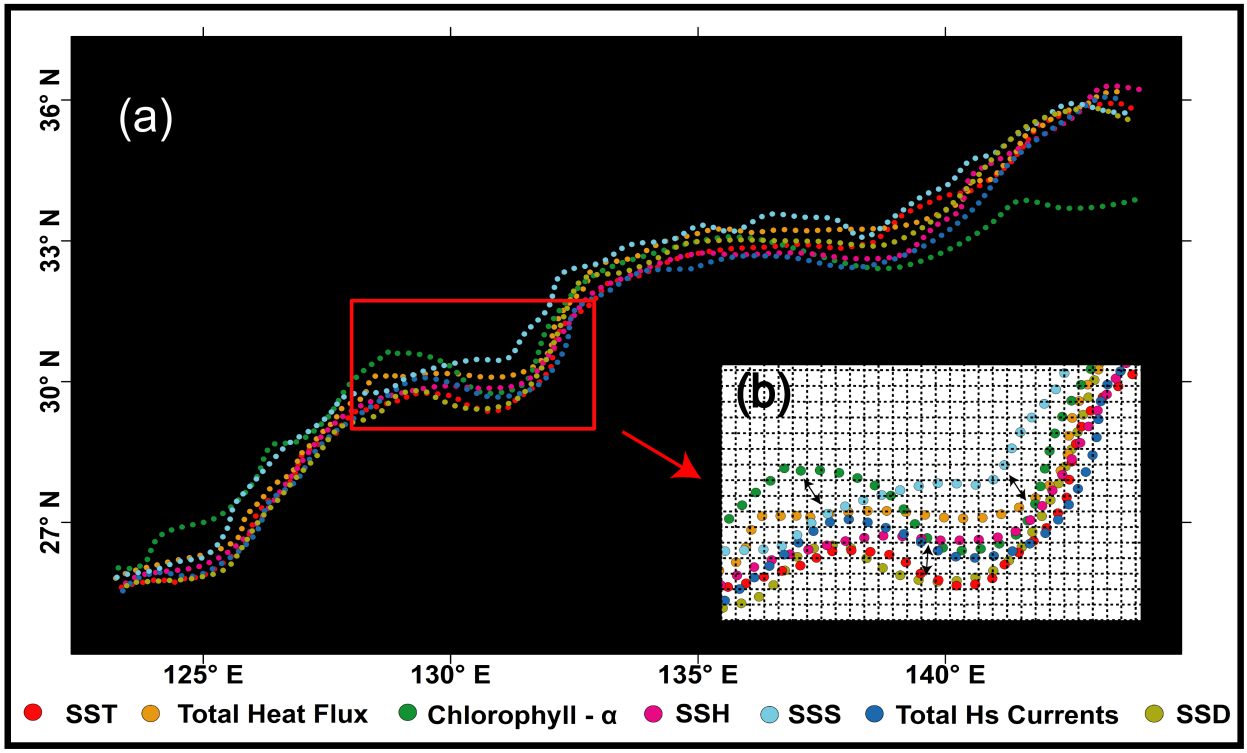

Figure 3. Depicts the computed midpoints from centerlines (**a**) location of vertex in similar column varying with rows; (**b**) sample zoomed segment from red box illustrating the grids from which the latitude and longitude were used to compute distance matrix and slope matrix to analyse spatial variation among the centerlines from all seven parameters.

3. Results

3.1. Mapping Kuroshio Ocean Front by Utilizing Methodology from Previous Related Studies

Initially, methods suggested by Wang [130] were employed to map the warm tongue of KC from SST climatology by defining an isotherm of 23 °C (Figure 4). Nevertheless, defining isotherm could not detect during summer as KC wears off due to uniform sea surface heating. The blue polygon (Figure 4) represents a region of Kuroshio warm tongue.

Later, we regenerated the results as per the algorithms proposed by Liu and Hou for detecting Kuroshio front from SST and chlorophyll-α [18] using a range between 25–27 °C (Figure 5a) and 0.02–0.4 mg m^{-3} (Figure 5b). The black box in Figure 5a represents the Kuroshio tongue, and the green color in Figure 5b shows the Kuroshio region. These algorithms were able to detect Kuroshio between Taiwan and Kyushu, and inferred that the shape of KC's extent is not conserved when applied to the datasets of this research.

However, the single value or algorithm did not yield the expected outcome. Therefore, we decided and tested the various combinations of image analysis techniques to find the most competent alliance of spatial filters, classification algorithms, raster queries, feature extraction approaches, and analysis methods to map and examine the interrelation between the Kuroshio centerline from daily data processed to weekly, seasonal and climatology (30, 32, 22, 26, 27, 27, 25, and 32 years) of total heat flux, SST, chlorophyll-α, SSH, SSS, SSD, sea surface current, and satellite-tracked Legrangian Argo drifter data, respectively.

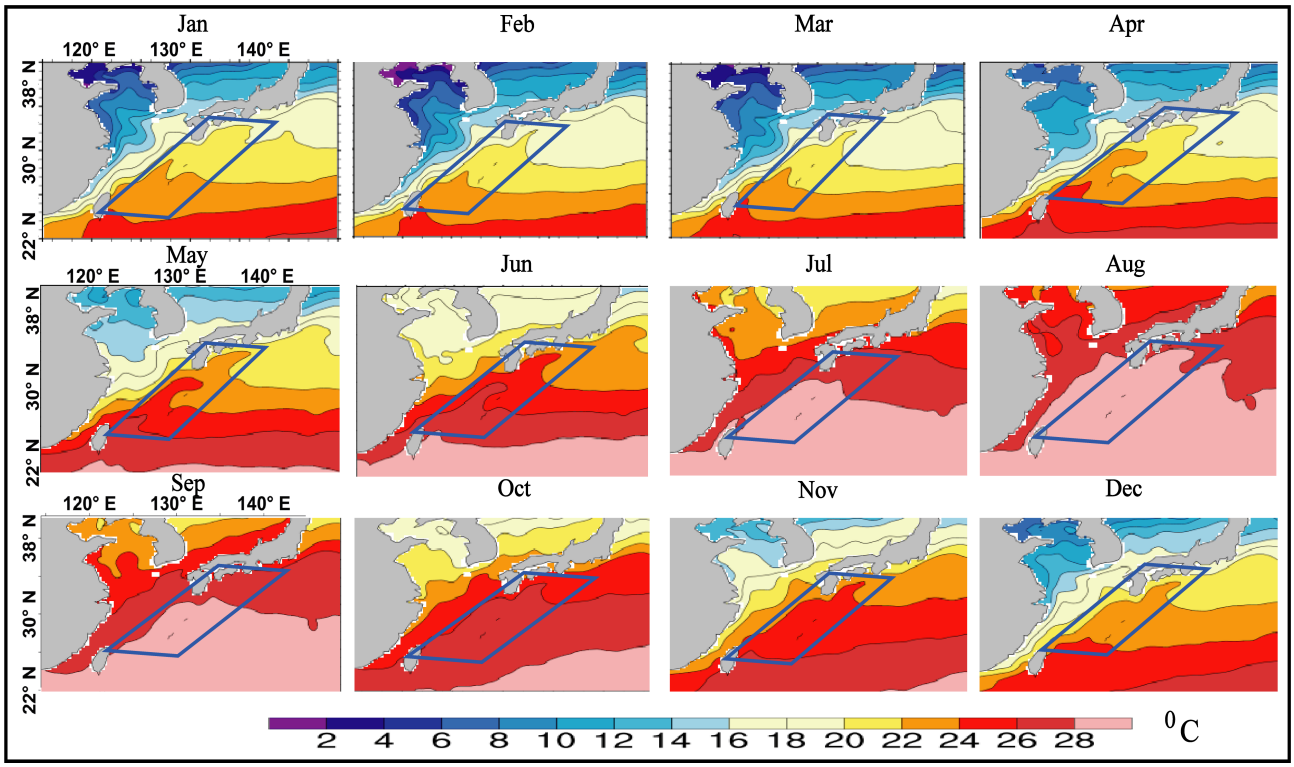

Figure 4. The SST climatology dispersal from 1993 to 2007. The blue polygon is a zone of Kuroshio warm tongue recreated for our study area using OISST version 2.0 by employing isotherm of 23 °C as per proposed by Wang et al. [130] .

This research, monthly climatological synoptic view of all the eight datasets with a fundamental image enhancement covering the study area between 20° to 40°N and 115° to 145°E, as illustrated in Figure 6.

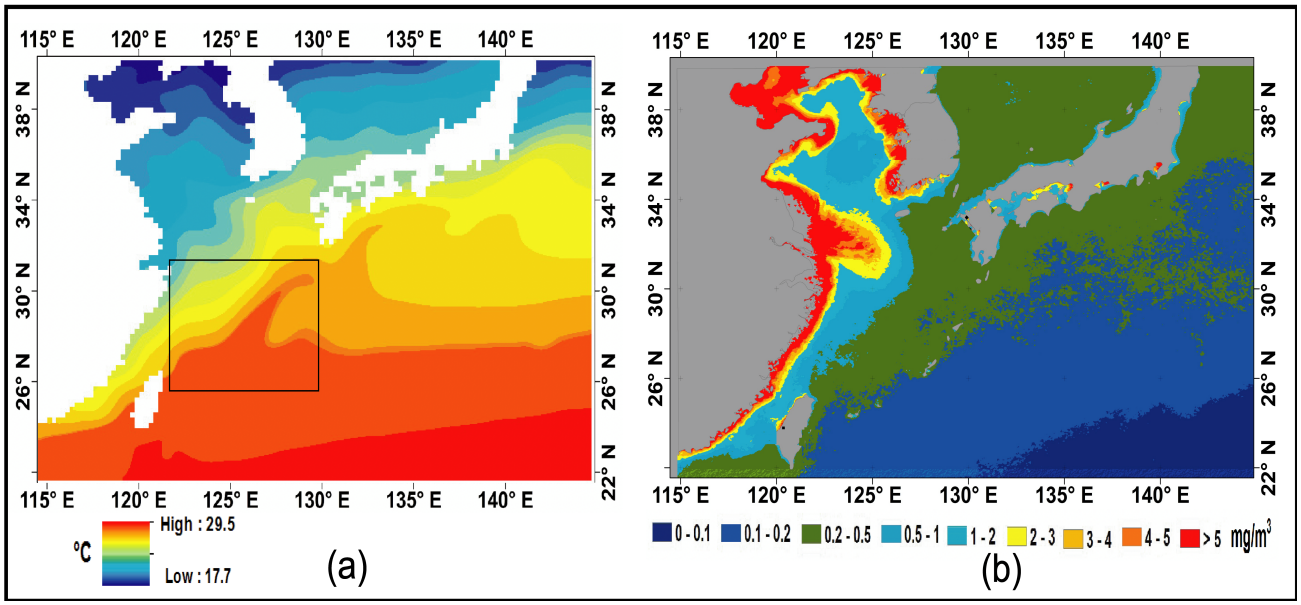

Figure 5. Climatological annual mean distributions recreated for our study area (**a**) SST from OISST version 2.0 between 2000–2009 illustrating isolines and Kuroshio warm tongue inside the black box; (**b**) Oceancolour Version 4.2 chlorophyll-α average from 1998–2010 to demarcate KC as per the methodology by Liu and Hou [18].

3.2. Detection of Kuroshio from Satellite Data

At the outset, we selected the datasets from their first day of availability. Then, those that do not start in January and end in December are filtered. Thus, while computing climatology (monthly) (Figure 4), all datasets have completed 12 months. Finally, we tested the selected algorithms on the area between 20° to 40°N and 115° to 145°E (Figure 1).

Satellite tracked Lagrangian Argo drifters widely used observational data physical oceanography to study and analyze the statistical dispersion properties of surface currents in both deep and continental edges in exceptional spatial resolution. The maturing data of Argos are from various oceanographic research programs, most of them focusing on Kuroshio and its contiguous neighborhoods. Moreover, data from numerous drifters are obliged to investigate the facade of ocean currents. Therefore, to study KC as per the previous studies, approximately data from 585 Argos and 120,000 observations are required.

Furthermore, the mathematical trajectory modeling for scientific applications is a demonstrative tool to calculate Lagrangian simulations. In this respect, mastery in understanding ocean currents is a must to simulate vivid trajectories [131]. On the other hand, remotely sensed sea surface current represents the combined east seawater velocity and meridional north seawater velocity components of geostrophic and Ekman currents. However, in this study, satellite rendered KC is correlated with Argo data by vying slope and distance from the origin (Figure 7). The calculated slope and distance from the origin using the coordinates (latitude and longitude) of midpoints from the centerlines of KC employing Argo and satellite-based sea surface current. Then, calculating the coordinates of the vertex in similar columns varies with rows. Figure 7a,b shows the KC centerline from Lagrangian drifters, and GlobCurrent exhibits a 95% similar spatial pattern between Taiwan and south of Japan with a distance less than 500 m. However, as we move upstream of KC from the south of Japan to the end, the spatial pattern correlation reduces to 75%, and variations of distance increases between 500 m to 1.5 km, in the various sections of KC, primarily from October–March.

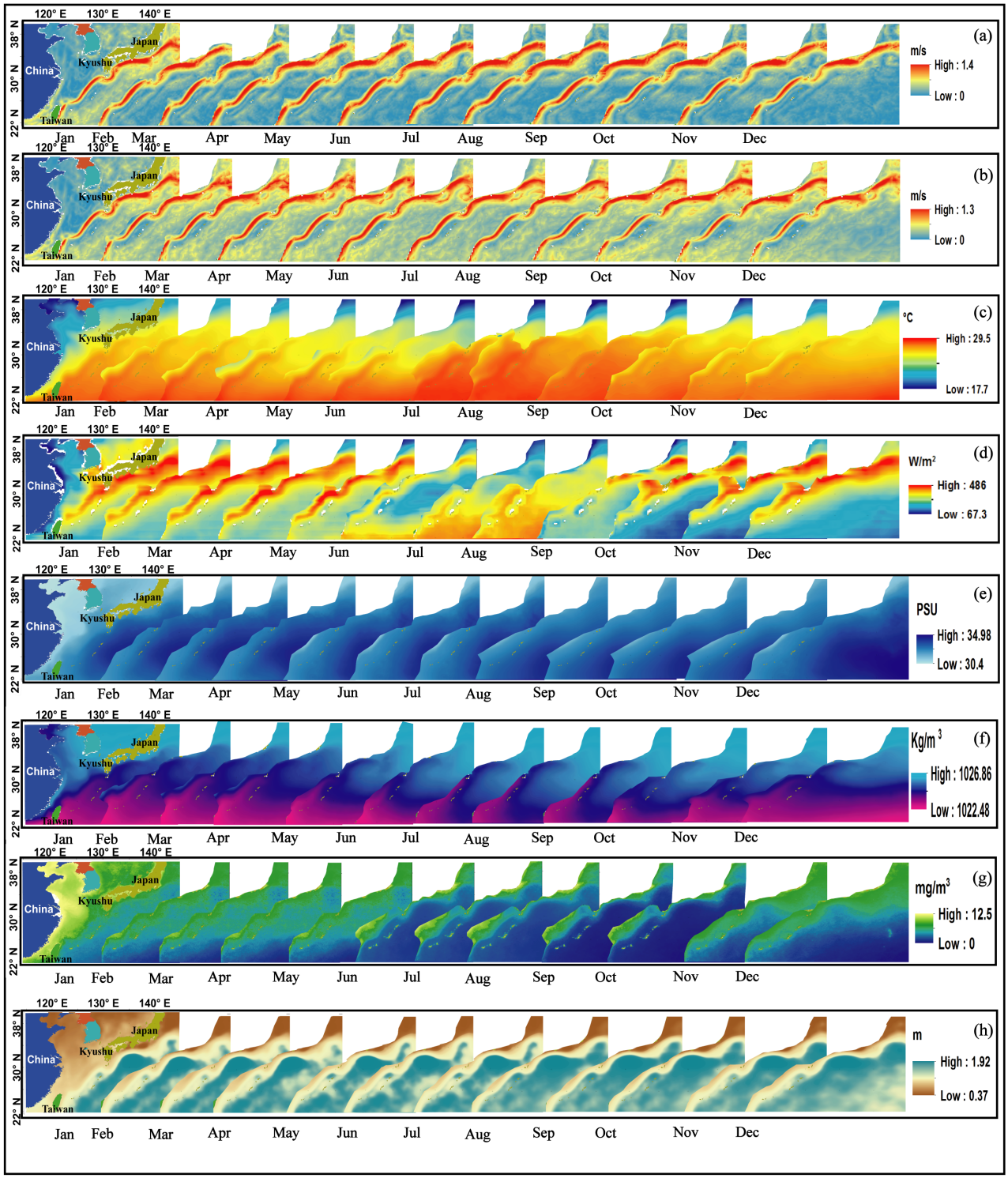

Figure 6. Synoptic view of data (**a**) Argo; (**b**) Sea Surface Current; (**c**) SST; (**d**) Heat Flux; (**e**) SSS; (**f**) SSD; (**g**) Chlorophyll-*α*; and (**h**) SSH illustrating entire KC by applying simple spatial filters .

Finally, the synoptic composition of the whole procedure applied for all the selected datasets and all months, especially for March, is illustrated in Figure 2. The Kuroshio extent and its centerline from monthly climatology data of sea surface current at 0 m between 1993 and 2018 (Figure 8a). The Kuroshio extent from their respective parameters used to extract the climatological Kuroshio as a polygon zone for March as shown in Figure 8b, whereas, in previous studies, KC was studied as a rectangular region or as a line feature.

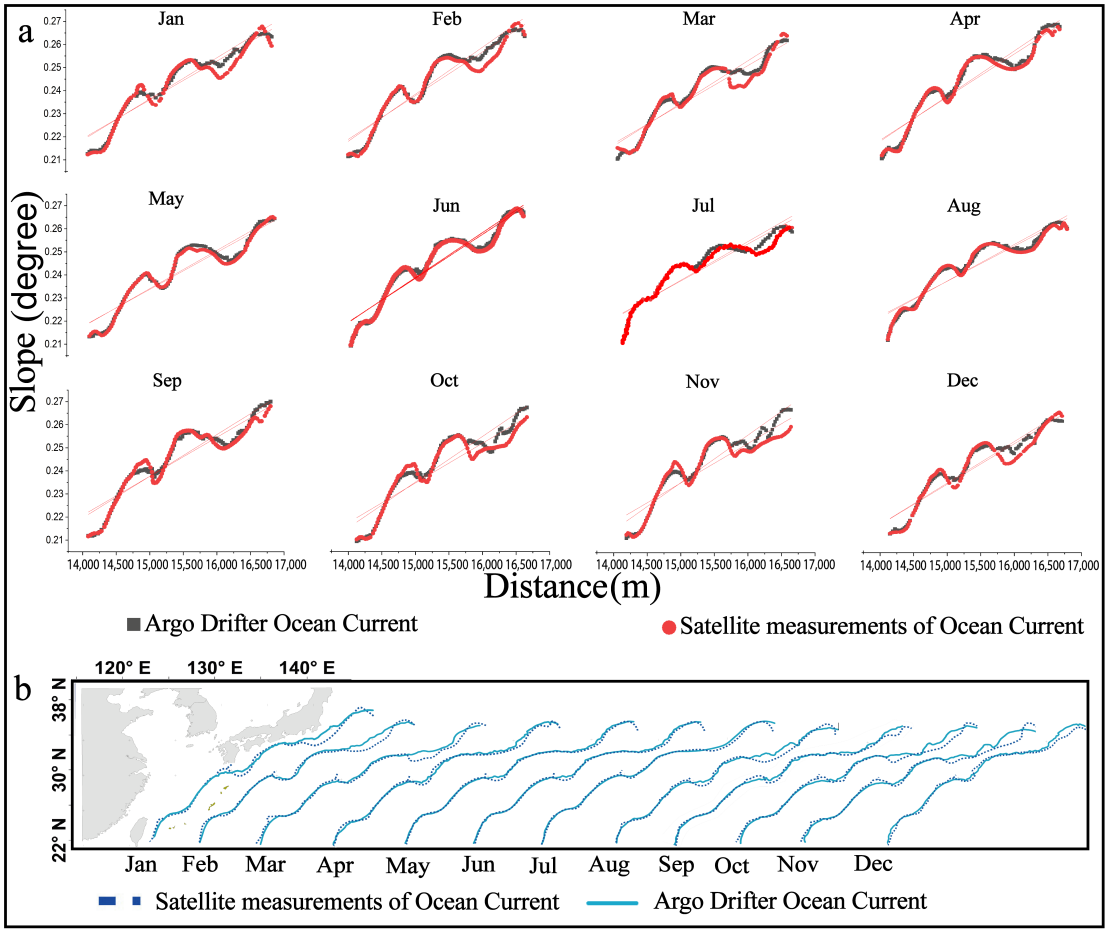

Figure 7. Correlation of KC from Argo drifter (grey) and Satellite rendered (red) (**a**) illustrates the variation in slope (degree) with distance (meter). (**b**) the climatological spatial variation among KC from drifters and satellite during 1993–2018 .

Minimum-maximum stretch, natural break classification, and feature extraction distinguish Kuroshio from its surrounding area. The 25 years mean climatological surface current velocity in the study area is from 0.1 to 1.3 ms^{-1}, whereas the standard deviation ranges between 0 to 0.6 ms^{-1}. The Kuroshio from the sea surface current data is used to validate the results from other parameters.

Figure 9a shows the overlay of the Kuroshio centerline obtained from long-term monthly climatological SST (red), heat flux (black), and sea surface current (dotted blue). The mean climatological of 32 years SST and 30 years heat flux is around 14.75 °C and 140 Wm^{-2}. The SST-based results are from a sequence following histogram equalization, convolution filter, and Laplacian filter, succeeded by feature extraction. Moreover, the sea flux data being a thermal component related to SST, revealed the centerline with a different combination of digital image analysis techniques similar to surface current (i.e., minimum-maximum stretch and natural break). Still, the sequence of applied algorithms was different (Figure 2).

Figure 9b illustrates a comparison of the centerline of sea surface current (dotted blue) Kuroshio with SSS (cyan) and SSD (brown). The minimum and maximum SSS and SSD from 27 years monthly long-term average data sets are 30.4 to 35 PSU and 1022.5 to 1027 kg m^{-3}. Surprisingly, both SSS and SSD yielded results by applying similar algorithms and in the same hierarchy. Suitable methods for SSS and SSD are standard deviation (n = 1) classification algorithms, including convolution, sharpening, and feature extraction.

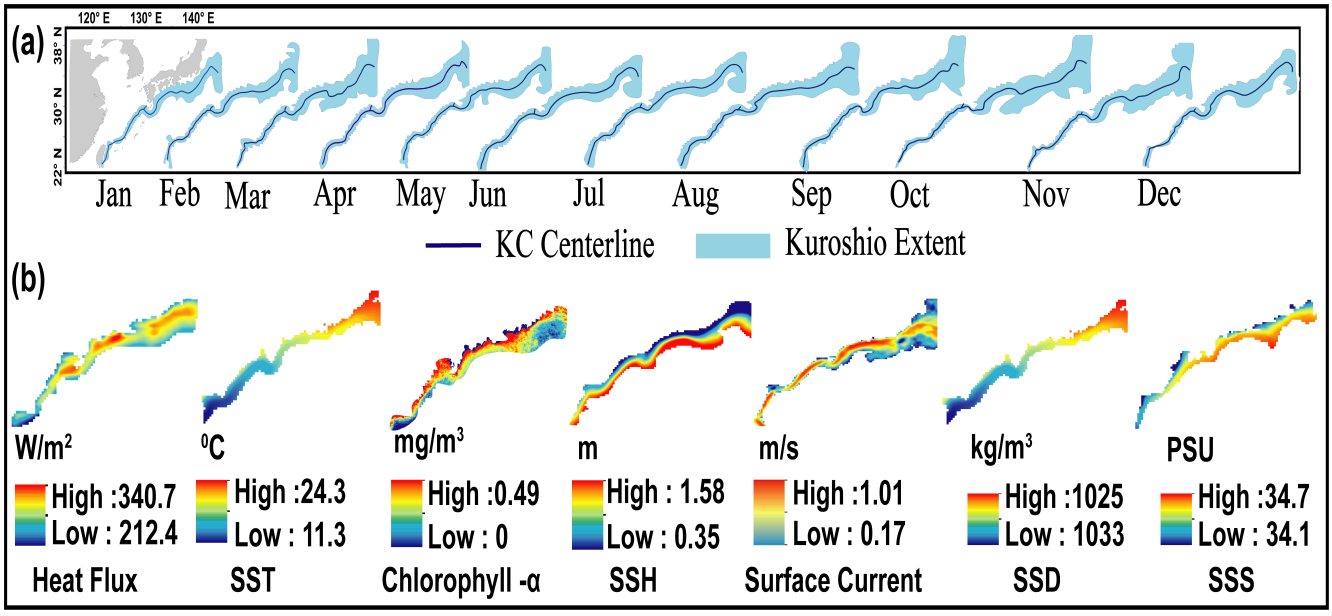

Figure 8. The climatological monthly dispersal (**a**) sea surface current data with Kuroshio extent and its centerline (1993–2018); (**b**) the Kuroshio extent from their respective parameters.

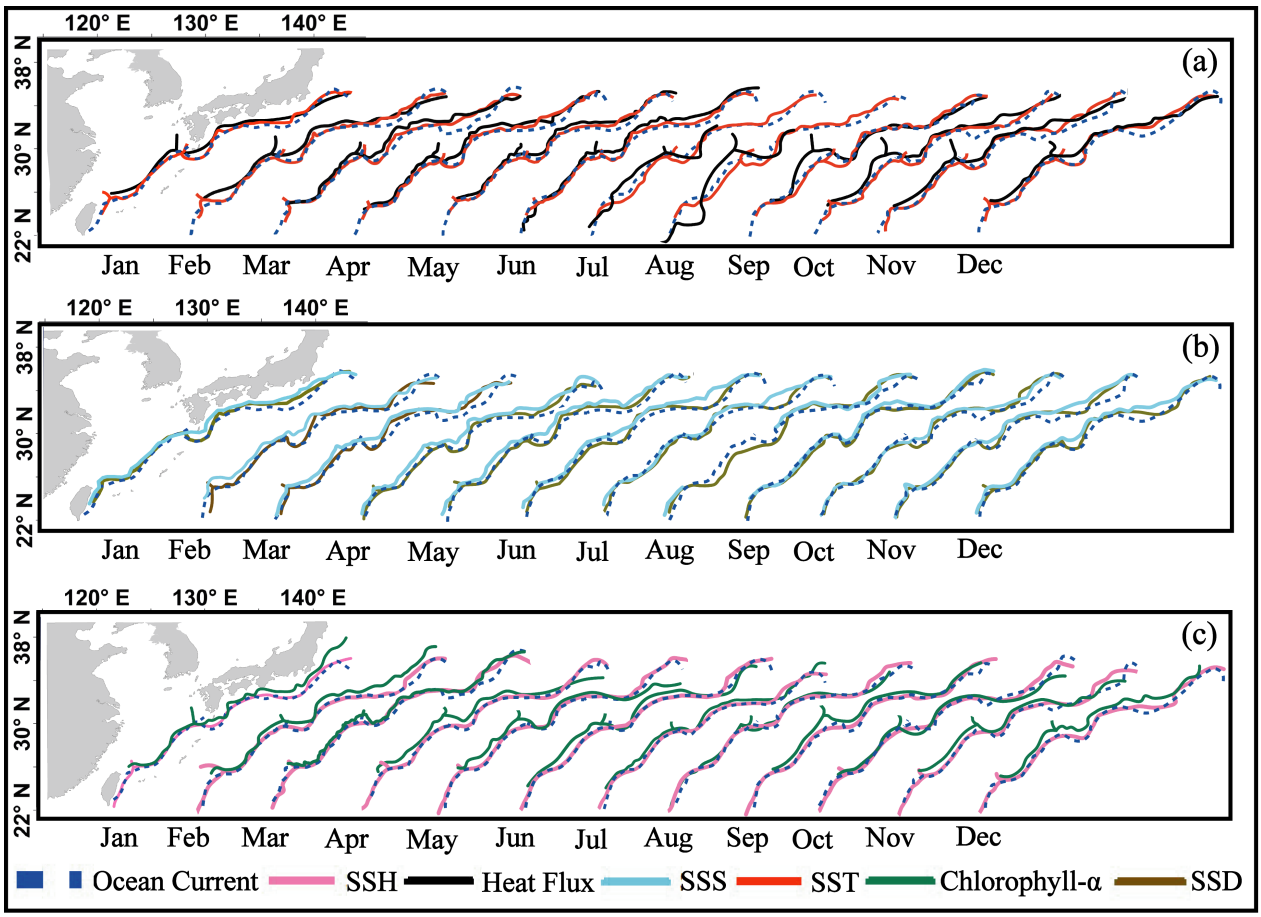

Figure 9. The KC centerline from monthly climatology (**a**) Sea Surface current (dotted blue) overlaid on SST (red) and Heat Flux (black); (**b**) comparison of Sea Surface current (dotted blue) with SSS (cyan) and SSD (brown); (**c**) Sea Surface current (dotted blue) with chlorophyll-*α* (green) and SSH (pink).

Figure 9c gives the synoptic view of results from chlorophyll-α (green), SSH (pink), and sea surface current (blue dotted). The range of chlorophyll-α from 26 years of monthly climatology is between 0 to 12.5 mg m^{-3}, with a higher concentration of chlorophyll-α is observed between the Mainland and Taiwan and Mainland and Japan. At the same time, the concentration is found to be minimum in the path where Kuroshio current flows. After applying minimum-maximum stretch in combination with a conditional filter, Kuroshio distinguished itself from its surroundings by retaining only the chlorophyll-α within 0 to 0.5 mg m^{-3}. The application of filters is followed by natural break data classification to further enhance the feature, finally with vectorization.

On the other hand, the 22 year average monthly from the sum of sea level anomaly and mean surface geoid is found to be 0.95 m. Furthermore, we extracted the Kuroshio centerline by applying a data classification algorithm of standard deviation ($n = 1$) followed by a north gradient filter and then feature extraction.

3.3. Inter-Comparison of Kuroshio Centerline from Climatology

Figure10a depicts the slope matrix in percentage. It represents the intercomparison of Kuroshio centerlines variation in Latitude with an increase in Longitude from Taiwan till Japan among seven selected parameters. The slope variation of one parameter is compared to another parameter using twenty-one combinations on the y-axis and climatological months on the x-axis. One percent variation in the slope represents 0.0087°. Thus, the slope matrix gives an accurate insight into how the path of Kuroshio fluctuates with one another on a monthly climatological scale using sharp color changes.

Figure 10b illustrates how far the centerline of Kuroshio spatially varies amongst selected seven parameters using the distance matrix. For example, one percent variation in the distance matrix equals 1.77 km. The distance is measured based on the interpretation of changes in the y-axis for every change in the x-axis. The usage of 252 combinations in total with obvious intensities to compare and associate the spatial distribution of the Kuroshio's centerline extract from heat flux, SST, SSS, SSD, chlorophyll-α, SSH, and sea surface current on a long term monthly scale.

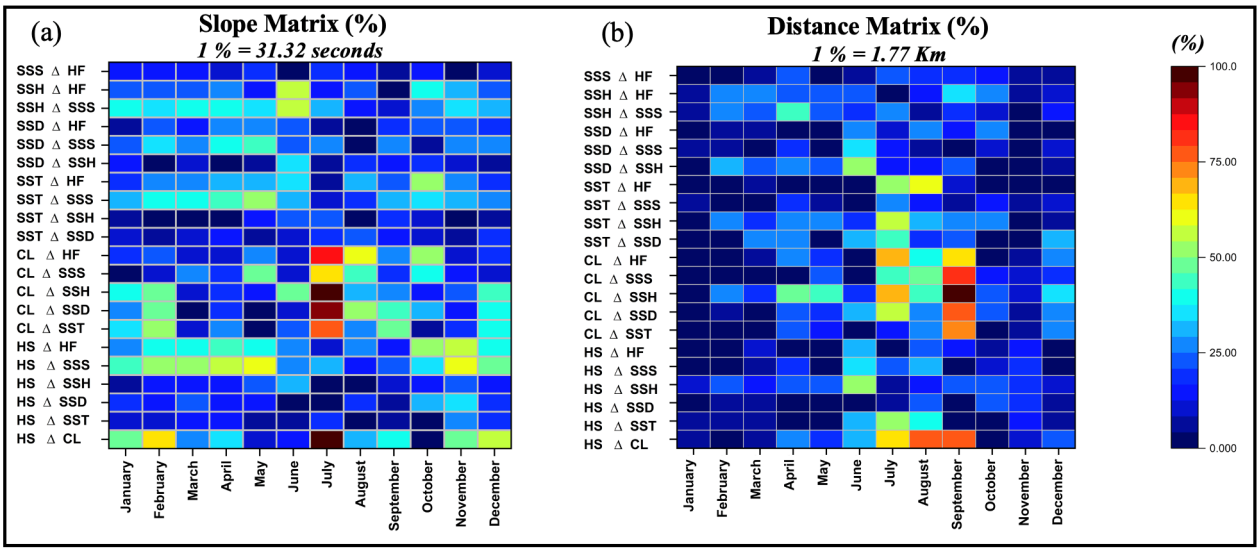

Figure 10. Inter-comparison of KC climatological centerline from heat flux (HF), SST, SSS, SSD, chlorophyll-α (CL), SSH, and sea surface current (HS) using (**a**) slope matrix; (**b**) distance matrix.

Figure 11 portrays the overlay projection of the centerlines from all parameters and all months. The length of the Kuroshio current was measured as 2818 km. However, the measured distance along the path, including curves and detours, was 3086 km. Then, elect five cross-sections considering the location where Koroshio tends to arc, progressing uninterrupted and at the end.

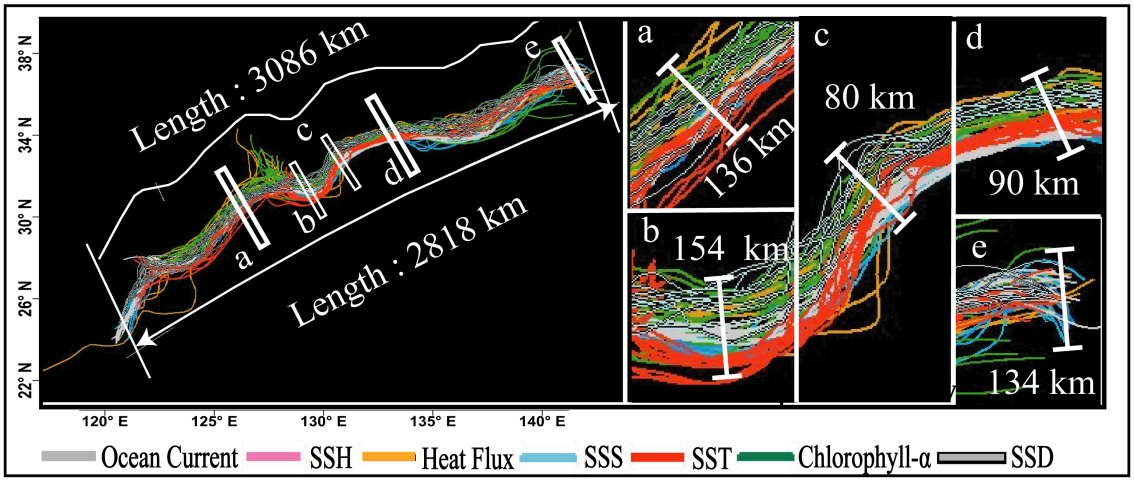

Figure 11. Kuroshio centerlines of all seven parameters to analyze the deviation from dominant path using five cross-sections at different locations where Kuroshio flows straight path (**a**,**c**,**d**), in 'U' shape (**b**) and its end point (**e**).

Figure 11a is the cross-section around Tokara Strait; the approximate variation among centerlines is 134 km, equivalent to a 4.5 pixel. The second cross-section (Figure 11b) is south of Kyushu, and, notably, Kuroshio takes a 'U-turn'. At this location, the deviation is 154 km. The following two cross-sections (Figure 11c,d) are selected 132.5°E, 31°N and 136°E, 33°N. In between these coordinates, Kuroshio tends to flow uninterrupted with a variation of 80 and 90 km. Finally, a cross-section at the end of the study area window (Figure 11e). Then, distance was measured between the condensed lines, which is 134 km, and by including those of Chlorophyll-α manifesting extreme shift is 177 km.

The standardized ratio of distance and slope variations showing their corresponding magnitude between the Kuroshio from sea surface current data and heat flux, SST, SSH, chlorophyll-α, SSH, SSS, and SSD are illustrated in the framework of Figure 12a,b. The statistics behind the normalization or non-dimensionalization is by dividing both the root mean difference and the standard deviation of the data set (in a column of model prediction) values by the standard deviation values of the observations. Then, the observation point is plotted along the x-axis at a unit distance from the origin, making it possible to plot statistics for different variables with different units on the same plot.

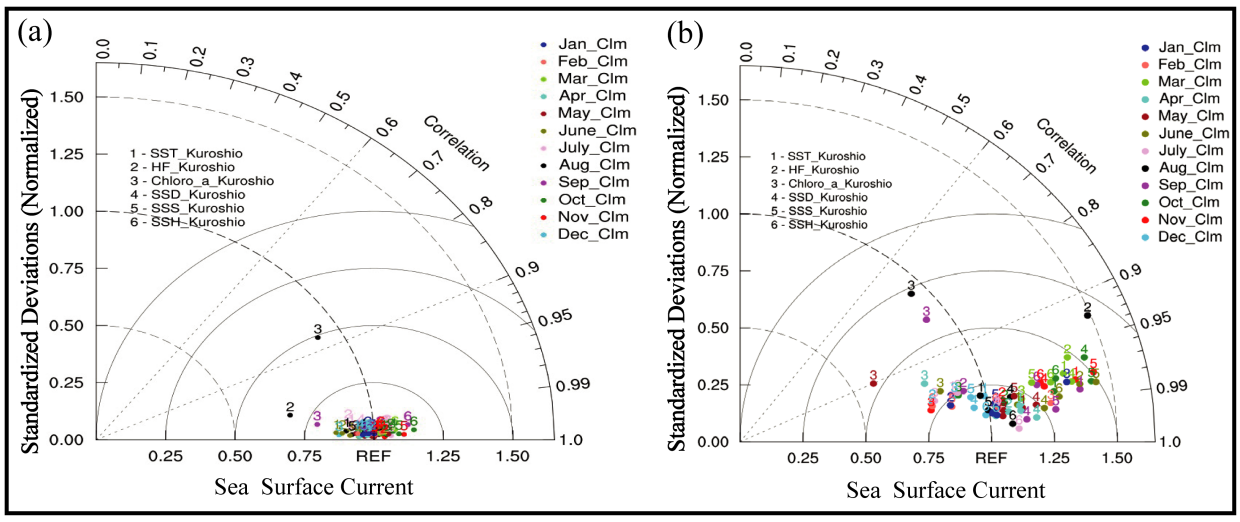

Figure 12. Illustrates the comparison of distance and slope of climatological heat flux (HF), SST, SSS, SSD, chlorophyll-α (CL) and SSH with sea surface current (REF = reference parameter) from their correlation and normalized standard deviations using (**a**) distance correlation; (**b**) slope correlation.

Furthermore, most of the case variance values (i.e., the normalized standard deviation of heat flux, SST, SSH, chlorophyll-α, SSH, SSS, SSD) and reference variance (sea surface current) computed from monthly climatology fall within 0.75 and 1.25 for distance (Figure 12a) and 0.5 and 1.5 in case of the slope (Figure 12b). Their respective case variance range is 0 to 0.2 (distance) and 0 to 0.45 (slope). Most of the cross-correlation coefficients of variance from SST, SSH, total heat flux, SSS, SSD, and chlorophyll-α parameters to sea surface current are under 0.99 for distance and 0.9 for slope.

3.4. Kuroshio from Weekly and Seasonal Data

Two extreme weather and climate events, such as typhoons and very strong El Nino, were selected to examine the refined combination of filters on weekly and seasonal scales to detect KC. Figure 13 illustrates the study area during typhoon Maria struck during 3–12 July 2018, plus six more days as the environment is uncertain with a coupling of various dynamic factors [132]. On a daily to weekly time scale from SSS and chlorophyll-α, the spatial signals of KC could not be identified and were very weak in SSD by the combination of filters. However, the combined spatial algorithms effectively unveiled the eddy's from sea surface current data on a small-time scale data set.

Figure 14 demonstrates the performance of filters to identify and extract KC during the winter season of very strong El-Nino in December 2015–February 2016. On a seasonal scale, the spatial pattern from SSS, chlorophyll-α, and SSD was also quite pale; hence, more iteration by the combination of the filter was employed on these datasets. Thus, data sets such as chlorophyll-α and SSS must be on a seasonal scale for effective mapping of sea surface current.

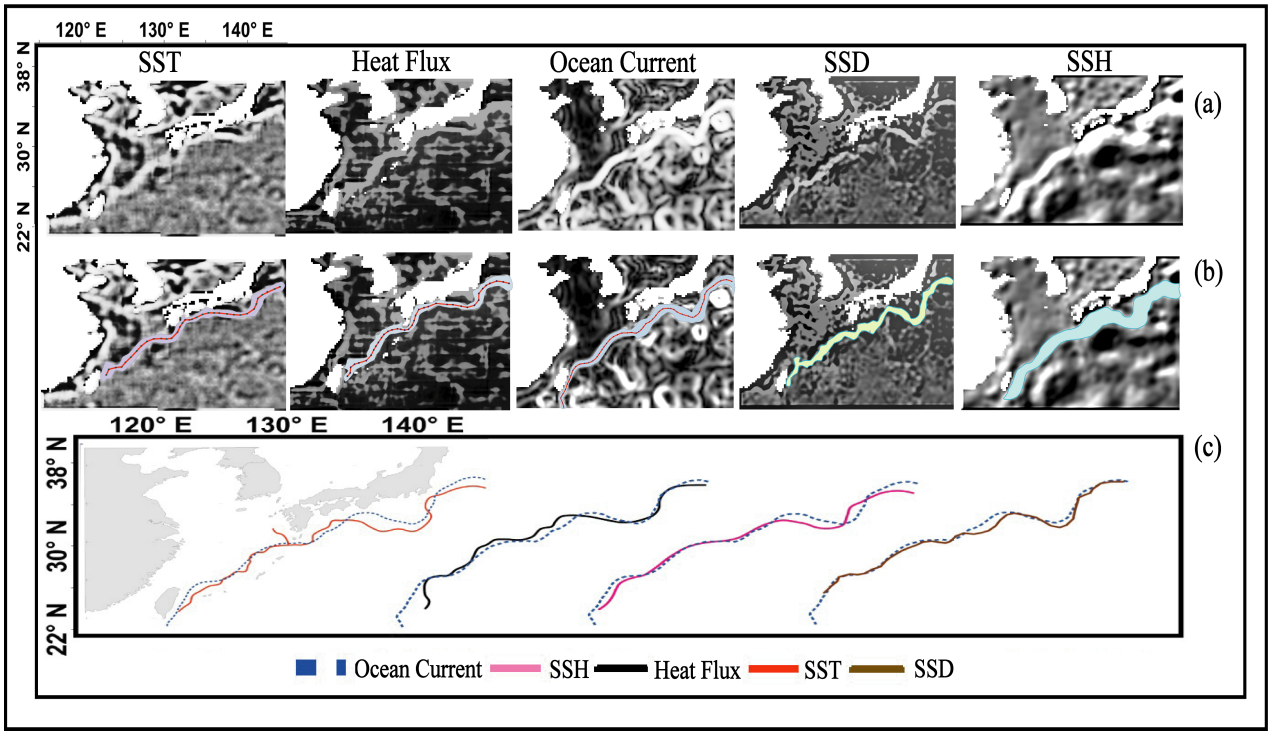

Figure 13. Daily to weekly time scale of satellite based oceanographic data set during typhoon Maria (3–12 July 2018, plus six more days) (**a**) unveiling of Kuroshio by applying combination of spatial filters; (**b**) extracted KC extent with centerline; (**c**) comparison of centerline with sea surface current(blue dotted).

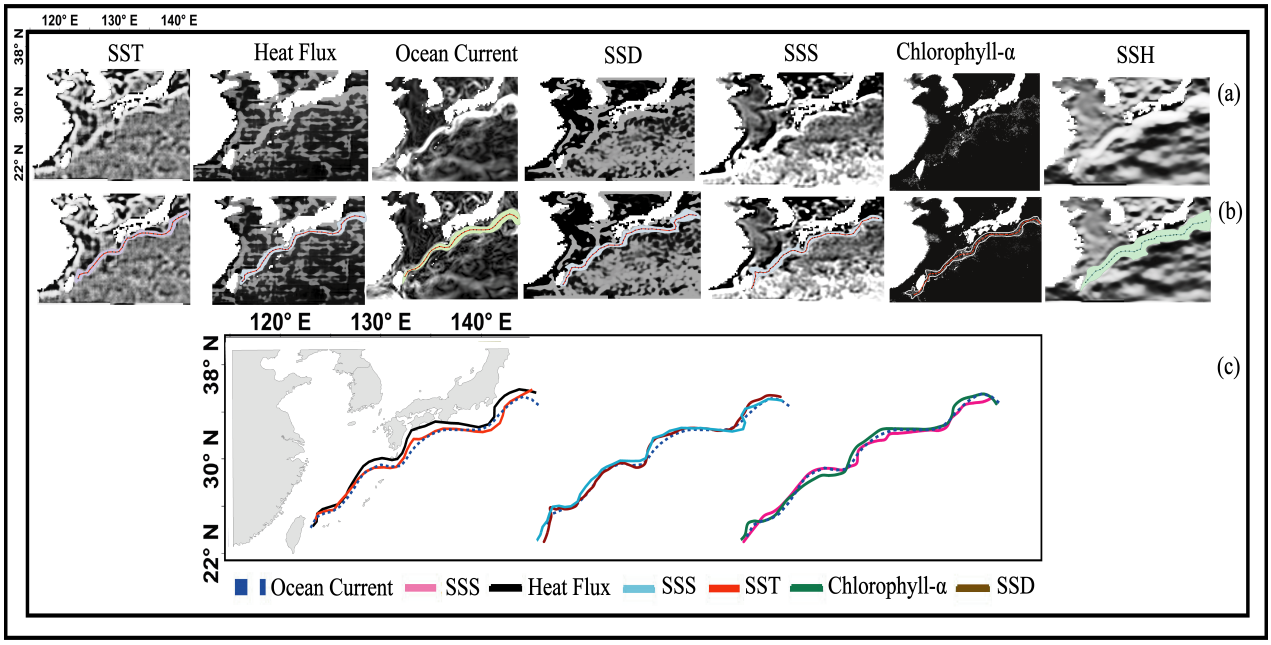

Figure 14. Daily to seasonal scale dispersal of remote sensing ocean parameters during very strong El-Nino between December 2015 to February 2016 (**a**) unveiling of Kuroshio; (**b**) extracted KC extent with centerline; (**c**) comparison of centerline with sea surface current (blue dotted).

4. Discussion

The results obtained by replicating existing methods [18,130] of using spectral range as shown in Figures 4 and 5 were able to disclose only the warm tongue [133], the KC extent, centerline, and its prevail undetected. Moreover, the Kuroshio extent is distinguished in spectral and visible from Argo [99], Satellite-derived ocean current [101] and SSH [114] by applying simple filters. At the same time, it fades off in summer (SST and HF) and remains invisible in other datasets Figure 6.

During the first part of the summer, the length of KC from SST and HF decreases and tours uninterrupted, possibly due to the seasonal uniform surface warming [18]. Hence, to unveil the Kuroshio extent and its centerline, the methodology proposed by combining various algorithms in this study, as shown in Figure 2, stands out. Using histogram equalization, convolution, and Laplacian filter on SST, to distinguish the KC from its surrounding water masses, even during the summer (Figure 15). It was incomprehensible for conventional ramps [18,130] to detect the weakening thermal signatures, which ultimately disappear due to ocean surface heating. Similarly, we could plot Kuroshio from Taiwan to Kyushu during summer with an exception in June by using heat flux data. However, during August, heat flux data show a loop in the northeast of Taiwan, possibly due to eddy formation, as illustrated in Figure 9a. The branch in northward dividing from the main path is related to Tsushima current, especially during December to March [134]. The slope variation between SST and sea flux is less than 30% in most months, indicating a similar spatial pattern, except for 50% in October. The KC identified from the Argo drifter [99] overall 85% correlates spatially with the satellite-based surface current but with variation observed in the south of Japan from October to March with 75% similarity in spatial structure. The Kuroshio extent from ocean current data [100] is narrow near Taiwan and gets wider as it flows along the east coast of Japan. Using our methodology, the results in Figures 8 and 9 show the Kuroshio path. Its centerline can be precisely distinguished from its surroundings in the North Pacific by a line feature from the east coast of Taiwan streaming northeastward.

In addition, the Kuroshio centerline plotted using thermal oceanographic parameters like SST, and total sea flux on ocean current does not overlap uniformly through its flow path (Figure 9a). Near Taiwan, all three parameters protrude most of the months.

During December, January, and February, the thermal constraints braid around 26°N and prolong northeast.

On the other hand, the distance between SST and heat flux reaches a maximum of 60% in July and August. The slope variation between SST and surface current-based Kuroshio is almost similar. The maximum distance between them is observed during July at nearly 85 km.

The salinity and density-based centerlines diffuse except for February in the north of Taiwan (Figure 9b). A deviation is observed between SSS and SSD around Tokara Strait. Our methodology could not detect SSS between 24°N and 30°N during August, maybe due to higher run-off inflow [135]. The slope and distance between Kuroshio from SSS and SSD is uniform, but 60% slope variation in May. SSS shows a notable slope deviation from ocean current through November to May. From Figure 9c, SSH overlay uniformly with Kuroshio from sea surface current. The chlorophyll-α centerline wiggles without a well-defined seasonal pattern indicate a distinct layer also in summer within waters of the continental shelf and the Kuroshio region [12–16].

A small bifurcation is observed from the main branch of chlorophyll-α, whereas clear and notable extensions are visible from SST; this discrepancy may happen from baroclinicity. The overall difference in the distance among SST and chlorophyll-a's Kuroshio is significantly less than three pixels except for September.

The observed maximum difference of slope and distance is in summer between chlorophyll-α and surface current. Except for the distance of chlorophyll-α and heat flux during August climatology, all other parameters are in good correlation with the sea surface current. At the same time, the correlation of slope amongst case variance of SST, SSH, total heat flux, SSS, SSD, and chlorophyll-α parameters and reference variance of surface current are in wide range but still within the correlation of 0.95. However, the chlorophyll-α and heat flux of August and September are between 0.8 and 0.95.

Figure 16a,b depict the overlay of all seven parameters on Kuroshio current mapped from 585 satellite-tracked Lagrangian Argo drifters for January and July, when the deviation is observed commonly.

The minimum and maximum 32 years monthly climatological velocity of ocean current from Argo drifters [99] in the study area is 0.1 and 1.4 ms^{-1}. Interestingly, proximity analysis found that the centerline from all seven parameters falls within the Kuroshio region(red) mapped from drifter data. However, more deviation in the centerlines is observed in July around Kyushu, Tokyo, and the Kuroshio current's northeast end.

The signatures of chlorophyll-α and SSS are undetected from a daily to a weekly dataset to extract KC. In contrast, identified distinct eddies around the south of Japan by applying the combination of filters discussed in methodology on sea surface current in Figure 13. Nevertheless, the filters performed uniformly on seasonal and climatological data sets. However, the signatures of SSS, SSD, and chlorophyll-α are very weak [12–16]; hence, more iterations are needed for the vectorization of KC. The computed deviation of the KC centerline uses the distance and slope (Table 2). The grey color highlights the maximum deviation, whereas 'No Data' indicates that KC was not effectively extracted from chlorophyll-α and SSS from a daily to weekly scale. The maximum deviation of 4 pixels is observed between SSD and other parameters except for seasonal chlorophyll-α. As expected, sea surface current (HS), SSH, and SST have a close spatial similarity.

Based on the analysis, oceanographic parameters like total heat flux, SST, chlorophyll-α, SSS, SSD, and SSH can also map to Kuroshio taking utmost care while selecting datasets for a particular season. Moreover, as the satellite-based ocean currents data are available from only 1993, another dataset as stand-alone or combined can be used as a proxy to map Kuroshio before 1993. Thus, the designed framework is suitable for this study's area of interest.

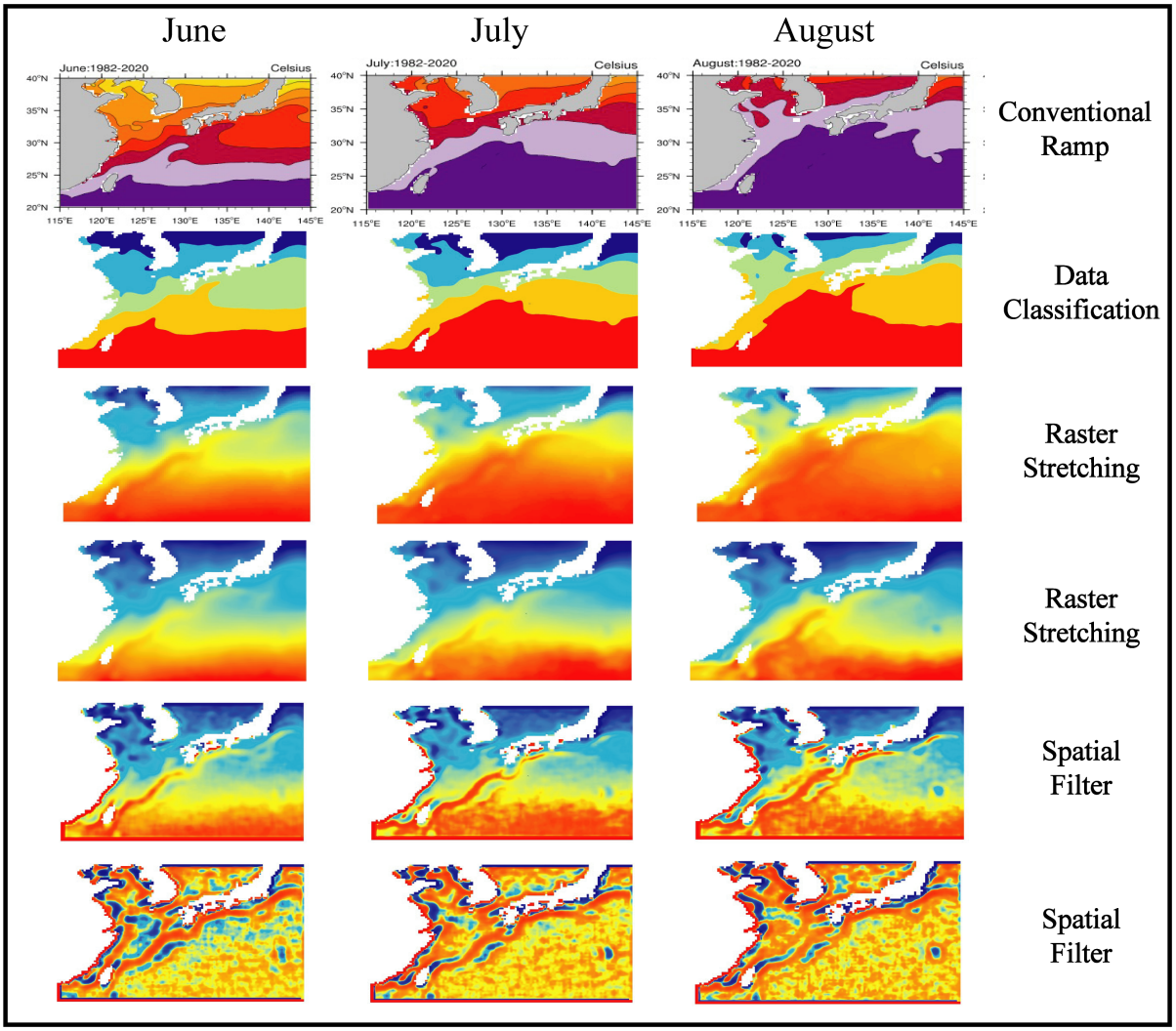

Figure 15. Unveiling Kuroshio from SST in various stages by the combination of spatial algorithms during summer.

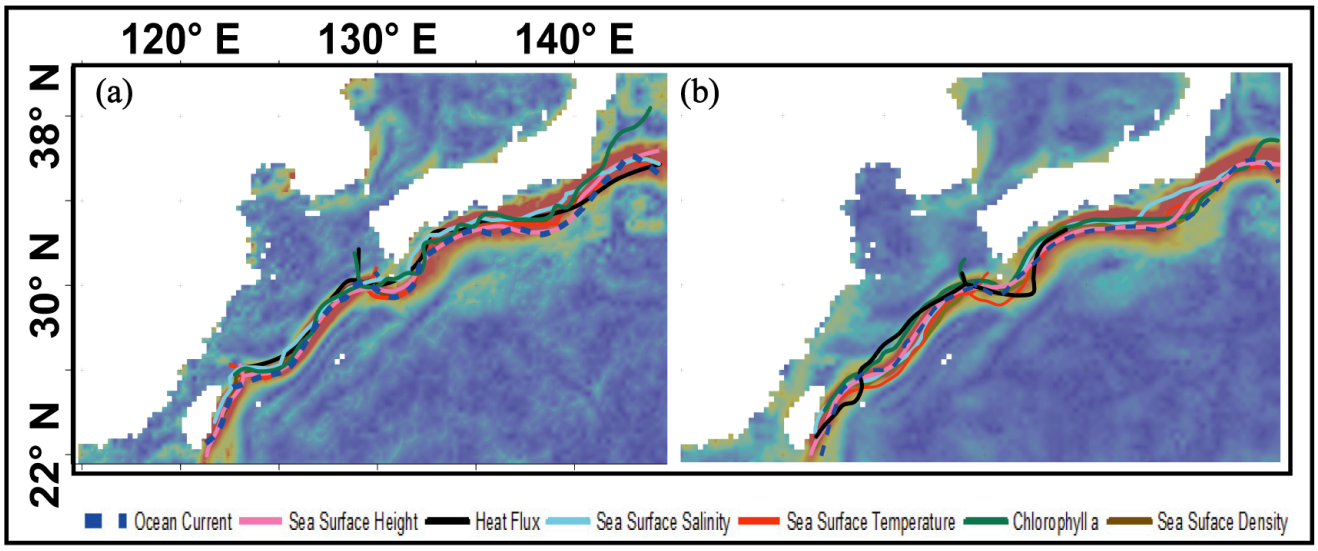

Figure 16. Kuroshio centerline from seven parameters overlay on Kuroshio from drifter data (**a**) January; (**b**) July.

Table 2. Comparison of deviation between the KC centerline from weekly and seasonal mean. The highlights in grey represents the parameters with maximum deviation.

Parameters	El-Nino(Seasonal) km	Maria(Weekly) km
HS △ chlorophyll-α	47.5	No Data
HS △ SST	29	9
HS △ SSD	71	100
HS △ SSH	50	0.3
HS △ SSS	63	No Data
HS △ HF	20.5	25
chlorophyll-α △ SST	76	No Data
chlorophyll-α △ SSD	23	No Data
chlorophyll-α △ SSH	2	No Data
chlorophyll-α △ SSS	15	No Data
chlorophyll-α △ HF	26	No Data
SST △ SSD	100.1	91
SST △ SSH	79	9
SST △ SSS	91	No Data
SST △ HF	50	18
SSD △ SSH	20	100
SSD △ SSS	8	No Data
SSD △ HF	50	73
SSH △ SSS	12	No Data
SSH △ HF	29	27
SSS △ HF	42	No Data

As for the chosen filters, their window size in pixel does not allow editing its kernel [10,11,61–85]. There are many potential configurations of filters and algorithms possible; deciding suitable candidates is an indispensable dilemma while determining whether to filter specific pixels or omit them intact in the window. It is worth mentioning that missing spectral signatures can be obtained from SST, chlorophyll-α, heat flux, SSS, SSD, SSH, sea surface current, and drifter data in the summertime by employing our framework. Then, during winter, the emerging thermal branches indicate the essential role of warm current overpowering the surface temperature evolution.

5. Conclusions

Although there are many studies on mapping Kuroshio [43,99,136–138], especially using remote sensing spatial filters [18,100,124,125,127], we have used all the oceanographic data to employ various digital image analysis filters. This research has reinforced the applicability of remote sensing satellite data to map ocean surface currents, especially Kuroshio.

The strategy incorporated multi-sensors from different satellites and a combination of spatial algorithms to increase the likelihood of extracting the centerline and extent of KC by demarcating from the surrounding water masses [1,75,138] of the East China Sea on the west and Pacific on its east. As input, 9490 to 13,505 daily images corresponding to between 26 to 37 years were used to compute monthly climatologies of SST, heat flux, chlorophyll-α, SSH, SSS, SSD, and sea surface current from both satellite and Argo drifters as in Figure 6.

Later, a suitable combination of spatial algorithms, filters, and conditions for each data set has been identified to extricate KC effectively. The novel perspective of this methodology is that it does not require a gradient threshold (objective value) depicted in Figure 2. In contrast, the conventional approach [18,130] employing isotherms, a single filter, and a simple indicator methodology cannot efficiently distinguish Kuroshio on the facade (Figures 4 and 5), notably throughout summer due to uniform heating, and it reappears in winter. In addition, the SST gradually diminishes from upstream to downstream. However, many studies [109–113] suggested that the missing summertime SST can be proxied using chlorophyll-α data. We

have manifested in this research that SST can be detected even during June, July, and August using a combination of spatial filters and algorithms (Figure 15).

The highlight is that, along with chlorophyll-α, a few other non-conventional datasets discussed in this study also provide the KC signature by retaining its shape as well. First, all the KC centerlines from SST, SSH, total heat flux, SSS, SSD, and chlorophyll-α oceanographic parameters were validated using 25 years satellite-based sea surface current (Figure 12) and then by correlating slope (Figure 10a) and distance (Figure 10b) using 252 combinations. Finally, these seven datasets were overlaid on the KC extracted from 32 years of satellite-tracked Argo drifted data to test their spatial proximity, as shown in Figure 16. Interestingly, the centerlines' deviation from the dominant path is no more than 2 pixels (Figure 11). Nevertheless, choosing spatial algorithms, dimensions of windows, and kernel methods for deciding proper candidates is a vital predicament, time-consuming, and not an easy chore.

To conclude, numerous investigations employed exclusively satellite-based sea surface current and drifter data as an ultimate source for studying KC [1,11,64–66,70,85,99,101,118,119]. This research additionally sheds light on the possibilities along with the surface current (satellite and drifters), SST, chlorophyll-α, and various other data sets (heat flux, SSH, SSD, and SSS) that can map KC, not only as centerline but also its extent as a polygon vector feature. Moreover, the results of one parameter can be used as a proxy to another on a long-term climatology and seasonal scale (92 images * 7 data sets).

Nevertheless, for weekly analysis on 16 images from five parameters (SST, sea surface current, HF, and SSD), altogether 80 images proved competitive by considering more iteration for vectorizing SSD. The results of the Kuroshio centerline illustrated in Figure 9 can help to monitor the seasonal and long-term spatio-temporal variation in addition to the analyses of physical and biological processes in the Kuroshio extent outlined by these various parameters and analyzing their interdependencies, inter variations on various time scales.

Author Contributions: Conceptualization: M.A.A.A. and S.-Y.L.; methodology: M.A.A.A. and S.-Y.L.; validation: M.A.A.A. and S.-Y.L.; formal analysis: M.A.A.A.; investigation: M.A.A.A.; resources: S.-Y.L.; writing—original draft preparation: M.A.A.A.; writing—review and editing: M.A.A.A. and S.-Y.L.; visualization: M.A.A.A.; supervision: M.A.A.A. and S.-Y.L.; project administration: S.-Y.L.; funding acquisition: S.-Y.L. All authors have read and agreed to the published version of the manuscript.

Funding: This research was funded by two projects: 1. Climate variability from monsoon Asia to future projection under Grant No. 110-2116-M-001 -006 and 2. Anthropogenic climate change–model development and CMIP6 participation under Grant No. 110-2123-M-001-003. A.S. Mohammed Abdul Athick is thankful to Academia Sinica, Taiwan for providing the graduate fellowship under Taiwan International Graduate Program (TIGP) in Earth System Science Program (ESS).

Institutional Review Board Statement: Not applicable.

Informed Consent Statement: Not applicable.

Data Availability Statement: All processed data, methodology, and filters presented in this research are available on request from the corresponding author for research purpose.

Acknowledgments: We would like to thank the Anthropogenic Climate Change Center, AC3 staff of RCEC, Academia Sinica for facilitating this research and to a lab mate Gagan Mandal. The authors also thank the anonymous referees for their helpful comments on this paper.

Conflicts of Interest: The authors declare no conflict of interest.

References

1. Caiyun, Z.; Ge, C. SST variations of the Kuroshio from AVHRR observation. *Chin. J. Oceanol. Limnol.* **2006**, *24*, 345–351. [CrossRef]
2. Nayak, R.; Mishra, S.; Satyesh Ghetiya, N.P.; Choudhury, S.; Seshasai, M. Remote Sensing Application in Satellite Oceanography. *Remote Sens.* **2018**, *93*, 156–165.
3. Takano, I.; Imawaki, S.; Kunishi, H. TS dynamic height calculation in the Kuroshio region. *La Mer* **1981**, *19*, 75–84.
4. Yamamoto, T.; Nishizawa, S.; Taniguchi, A. Formation and retention mechanisms of phytoplankton peak abundance in the Kuroshio front. *J. Plankton Res.* **1988**, *10*, 1113–1130. [CrossRef]

5. Saito, H. The Kuroshio: Its recognition, scientific activities and emerging issues. In *Kuroshio Current: Physical, Biogeochemical, and Ecosystem Dynamics*; Geophysical Monograph Series 243; American Geophysical Union: Washington, DA, USA, 2019; pp. 1–11.
6. Kawamura, H.; Mizuno, K.; Toba, Y. Formation process of a warm-core ring in the Kuroshio-Oyashio frontal zone—December 1981–October 1982. *Deep. Sea Res. Part A Oceanogr. Res. Pap.* **1986**, *33*, 1617–1640. [CrossRef]
7. Toda, T. Movement of the surface front induced by Kuroshio frontal eddy. *J. Geophys. Res. Ocean.* **1993**, *98*, 16331–16339. [CrossRef]
8. Yuan, D.; Han, W.; Hu, D. Surface Kuroshio path in the Luzon Strait area derived from satellite remote sensing data. *J. Geophys. Res. Ocean.* **2006**, *111*. [CrossRef]
9. Ji, C.; Zhang, Y. Investigation of the Chlorophyll-A Concentration Response to Sea Surface Temperature (SST) in the East China Sea. In Proceedings of the IGARSS 2019–2019 IEEE International Geoscience and Remote Sensing Symposium, Yokohama, Japan, 28 July–2 August 2019; pp. 8003–8006.
10. Hickox, R.; Belkin, I.; Cornillon, P.; Shan, Z. Climatology and seasonal variability of ocean fronts in the East China, Yellow and Bohai Seas from satellite SST data. *Geophys. Res. Lett.* **2000**, *27*, 2945–2948. [CrossRef]
11. Ullman, D.S.; Cornillon, P.C. Satellite-derived sea surface temperature fronts on the continental shelf off the northeast US coast. *J. Geophys. Res. Ocean.* **1999**, *104*, 23459–23478. [CrossRef]
12. Legeckis, R.; Brown, C.W.; Chang, P.S. Geostationary satellites reveal motions of ocean surface fronts. *J. Mar. Syst.* **2002**, *37*, 3–15. [CrossRef]
13. Marumo, R. Diatom plankton in the south of Cape Shionomisaki in 1953. *Oceanogr. Mag.* **1954**, *6*, 145.
14. Kawarada, Y. Diatoms in the Kuroshio waters neighboring Japan. *Inform. Bull. Planktol. Jpn.* **1965**, *12*, 8–16.
15. Kuroda, K. Chlorophyll distribution in the Kuroshio region, south of Japan. Kousuiken Note. *Sora Umi* **1987**, *9*, 19–29.
16. Imai, M. Seasonal variation of chlorophyll-a in the seas around Japan. *Oceanogr. Mag.* **1988**, *38*, 23–32.
17. Hanzawa, M. Studies on the mechanism of formation of cold water in the Okhotsk Sea. In *Report of Joint-Research on the Okhotsk Sea*; Research Coordination Bureau, Science and Technology Agency Tokyo: Kawaguchi, Japan, 1981; pp. 66–131.
18. Liu, Z.; Hou, Y. Kuroshio Front in the East China sea from satellite SST and remote sensing data. *IEEE Geosci. Remote Sens. Lett.* **2011**, *9*, 517–520. [CrossRef]
19. Nagai, T.; Otsuka, K.; Nakano, H. The Research Advancements and Historical Episodes brought by the Kuroshio Flowing across Generations. In *Kuroshio Current: Physical, Biogeochemical, and Ecosystem Dynamics*; American Geophysical Union (AGU): Washington, DC, USA, 2019; pp. 13–22. [CrossRef]
20. Garcia-Eidell, C.; Comiso, J.C.; Dinnat, E.; Brucker, L. Sea surface salinity distribution in the Southern Ocean as observed from space. *J. Geophys. Res. Ocean.* **2019**, *124*, 3186–3205. [CrossRef]
21. Su, F.C.; Tseng, R.S.; Ho, C.R.; Lee, Y.H.; Zheng, Q. Detecting surface Kuroshio front in the Luzon strait from multichannel satellite data using neural networks. *IEEE Geosci. Remote Sens. Lett.* **2010**, *7*, 718–722. [CrossRef]
22. Douglas, B.; McAdoo, D.; Cheney, R. Oceanographic and geophysical applications of satellite altimetry. *Rev. Geophys.* **1987**, *25*, 875–880. [CrossRef]
23. Fu, L.L.; Cheney, R.E. Application of satellite altimetry to ocean circulation studies: 1987–1994. *Rev. Geophys.* **1995**, *33*, 213–223. [CrossRef]
24. Fu, L.L.; Christensen, E.J.; Yamarone, C.A., Jr.; Lefebvre, M.; Menard, Y.; Dorrer, M.; Escudier, P. TOPEX/POSEIDON mission overview. *J. Geophys. Res. Ocean.* **1994**, *99*, 24369–24381. [CrossRef]
25. Lagerloef, G.S.; Mitchum, G.T.; Lukas, R.B.; Niiler, P.P. Tropical Pacific near-surface currents estimated from altimeter, wind, and drifter data. *J. Geophys. Res. Ocean.* **1999**, *104*, 23313–23326. [CrossRef]
26. Imawaki, S.; Uchida, H.; Ichikawa, H.; Fukasawa, M.; Umatani, S.i.; Group, A. Satellite altimeter monitoring the Kuroshio transport south of Japan. *Geophys. Res. Lett.* **2001**, *28*, 17–20. [CrossRef]
27. Ma, C.; Wu, D.; Lin, X. Variability of surface velocity in the Kuroshio Current and adjacent waters derived from Argos drifter buoys and satellite altimeter data. *Chin. J. Oceanol. Limnol.* **2009**, *27*, 208–217. [CrossRef]
28. Liu, Z.; Wu, L. Atmospheric Response to North Pacific SST: The Role ofOcean–Atmosphere Coupling. *J. Clim.* **2004**, *17*, 1859–1882. [CrossRef]
29. Konda, M.; Imasato, N.; Shibata, A. A new method to determine near-sea surface air temperature by using satellite data. *J. Geophys. Res. Ocean.* **1996**, *101*, 14349–14360. [CrossRef]
30. Murakami, H.; Kawamura, H. Relations between sea surface temperature and air-sea heat flux at periods from 1 day to 1 year observed at ocean buoy stations around Japan. *J. Oceanogr.* **2001**, *57*, 565–580. [CrossRef]
31. Kubota, M.; Kano, A.; Muramatsu, H.; Tomita, H. Intercomparison of various surface latent heat flux fields. *J. Clim.* **2003**, *16*, 670–678. [CrossRef]
32. Qiu, B.; Chen, S.; Hacker, P. Synoptic-scale air–sea flux forcing in the western North Pacific: Observations and their impact on SST and the mixed layer. *J. Phys. Oceanogr.* **2004**, *34*, 2148–2159. [CrossRef]
33. Frankignoul, C.; Sennéchael, N. Observed influence of North Pacific SST anomalies on the atmospheric circulation. *J. Clim.* **2007**, *20*, 592–606. [CrossRef]
34. Bond, N.A.; Cronin, M.F. Regional weather patterns during anomalous air–sea fluxes at the Kuroshio Extension Observatory (KEO). *J. Clim.* **2008**, *21*, 1680–1697. [CrossRef]

35. Konda, M.; Ichikawa, H.; Tomita, H.; Cronin, M.F. Surface heat flux variations across the Kuroshio Extension as observed by surface flux buoys. *J. Clim.* **2010**, *23*, 5206–5221. [CrossRef]
36. Cancet, M.; Griffin, D.; Cahill, M.; Chapron, B.; Johannessen, J.; Donlon, C. Evaluation of GlobCurrent surface ocean current products: A case study in Australia. *Remote Sens. Environ.* **2019**, *220*, 71–93. [CrossRef]
37. Rio, M.H.; Mulet, S.; Picot, N. Beyond GOCE for the ocean circulation estimate: Synergetic use of altimetry, gravimetry, and in situ data provides new insight into geostrophic and Ekman currents. *Geophys. Res. Lett.* **2014**, *41*, 8918–8925. [CrossRef]
38. Ablain, M.; Cazenave, A.; Larnicol, G.; Balmaseda, M.; Cipollini, P.; Faugère, Y.; Fernandes, M.; Henry, O.; Johannessen, J.; Knudsen, P.; et al. Improved sea level record over the satellite altimetry era (1993–2010) from the Climate Change Initiative project. *Ocean. Sci.* **2015**, *11*, 67–82. [CrossRef]
39. Nkwinkwa Njouodo, A.S.; Koseki, S.; Keenlyside, N.; Rouault, M. Atmospheric signature of the Agulhas Current. *Geophys. Res. Lett.* **2018**, *45*, 5185–5193. [CrossRef]
40. Sun, X. Analysis of the surface path of the Kuroshio in the East China Sea. In *Essays on Investigation of Kuroshio*; Ocean Press: Beijing, China, 1987; pp. 1–14.
41. Kawabe, M. Spectral properties of sea level and time scales of Kuroshio path variations. *J. Oceanogr. Soc. Jpn.* **1987**, *43*, 111–123. [CrossRef]
42. Kawabe, M. Variations of current path, velocity, and volume transport of the Kuroshio in relation with the large meander. *J. Phys. Oceanogr.* **1995**, *25*, 3103–3117. [CrossRef]
43. Akitomo, K.; Masuda, S.; Awaji, T. Kuroshio path variation south of Japan: Stability of the paths in a multiple equilibrium regime. *Oceanogr. Lit. Rev.* **1997**, *44*, 1226–1227.
44. Yamashiro, T.; Kawabe, M. Variations of the Kuroshio axis south of Kyushu in relation to the large meander of the Kuroshio. *J. Oceanogr.* **2002**, *58*, 487–503. [CrossRef]
45. Maximenko, N. Index and composites of the Kuroshio meander south of Japan. *J. Oceanogr.* **2002**, *58*, 639–649. [CrossRef]
46. Ebuchi, N.; Hanawa, K. Influence of mesoscale eddies on variations of the Kuroshio path south of Japan. *J. Oceanogr.* **2003**, *59*, 25–36. [CrossRef]
47. Nagano, A.; Kawabe, M. Monitoring of generation and propagation of the Kuroshio small meander using sea level data along the southern coast of Japan. *J. Oceanogr.* **2004**, *60*, 879–892. [CrossRef]
48. Usui, N.; Tsujino, H.; Fujii, Y.; Kamachi, M. Short-range prediction experiments of the Kuroshio path variabilities south of Japan. *Ocean. Dyn.* **2006**, *56*, 607–623. [CrossRef]
49. Takahashi, W.; Kawamura, H. Detection method of the Kuroshio front using the satellite-derived chlorophyll—A images. *Remote Sens. Environ.* **2005**, *97*, 83–91. [CrossRef]
50. Savchenko, V.K.; Bychkov, A.S.; Ilyichev, V.I. Kuroshio meandering and eddy formation to the East of Taiwan and their reflection in Potassium fields. *Terr. Atmos. Ocean. Sci.* **1995**, *6*, 1–11. [CrossRef]
51. Nishimura, T.; Kobayashi, T.; Tanaka, S.; Sugimura, T. Satellite monitoring of oceanic turbulence around Japan Islands. *Adv. Space Res.* **1995**, *16*, 137–140. [CrossRef]
52. Tang, T.; Tai, J.; Yang, Y. The flow pattern north of Taiwan and the migration of the Kuroshio. *Cont. Shelf Res.* **2000**, *20*, 349–371. [CrossRef]
53. Liang, W.D.; Tang, T.; Yang, Y.; Ko, M.; Chuang, W.S. Upper-ocean currents around Taiwan. *Deep. Sea Res. Part II Top. Stud. Oceanogr.* **2003**, *50*, 1085–1105. [CrossRef]
54. Tomita, H.; Kubota, M. Increase in turbulent heat flux during the 1990s over the Kuroshio/Oyashio extension region. *Geophys. Res. Lett.* **2005**, *32*. [CrossRef]
55. Mariano, A.J.; Griffa, A.; Özgökmen, T.M.; Zambianchi, E. Lagrangian analysis and predictability of coastal and ocean dynamics 2000. *J. Atmos. Ocean. Technol.* **2002**, *19*, 1114–1126. [CrossRef]
56. Beardsley, R.C.; Limeburner, R.; Owens, W.B. Drifter measurements of surface currents near Marguerite Bay on the western Antarctic Peninsula shelf during austral summer and fall, 2001 and 2002. *Deep. Sea Res. Part II Top. Stud. Oceanogr.* **2004**, *51*, 1947–1964. [CrossRef]
57. Tseng, C.T.; Sun, C.L.; Yeh, S.Z.; Chen, S.C.; Liu, D.C.; Su, W.C. The Kuroshio variations from satellite-derived sea surface temperature and Argos satellite-tracking Lagrangian drifters. *Int. J. Remote Sens.* **2011**, *32*, 8725–8746. [CrossRef]
58. Poulain, P.M.; Zambianchi, E. Surface circulation in the central Mediterranean Sea as deduced from Lagrangian drifters in the 1990s. *Cont. Shelf Res.* **2007**, *27*, 981–1001. [CrossRef]
59. Hsin, Y.C.; Wu, C.R.; Shaw, P.T. Spatial and temporal variations of the Kuroshio east of Taiwan, 1982–2005: A numerical study. *J. Geophys. Res. Ocean.* **2008**, *113*. [CrossRef]
60. Oka, E.; Kawabe, M. Dynamic structure of the Kuroshio south of Kyushu in relation to the Kuroshio path variations. *J. Oceanogr.* **2003**, *59*, 595–608. [CrossRef]
61. Canny, J. A computational approach to edge detection. *IEEE Trans. Pattern Anal. Mach. Intell.* **1986**, *PAMI-8*, 679–698. [CrossRef]
62. Holyer, R.J.; Peckinpaugh, S.H. Edge detection applied to satellite imagery of the oceans. *IEEE Trans. Geosci. Remote Sens.* **1989**, *27*, 46–56. [CrossRef]
63. Cayula, J.F.; Cornillon, P.; Holyer, R.; Peckinpaugh, S. Comparative study of two recent edge-detection algorithms designed to process sea-surface temperature fields. *IEEE Trans. Geosci. Remote Sens.* **1991**, *29*, 175–177. [CrossRef]
64. Cayula, J.F.; Cornillon, P. Edge detection algorithm for SST images. *J. Atmos. Ocean. Technol.* **1992**, *9*, 67–80. [CrossRef]

65. Cayula, J.F.; Cornillon, P. Multi-image edge detection for SST images. *J. Atmos. Ocean. Technol.* **1995**, *12*, 821–829. [CrossRef]
66. Cayula, J.F.; Cornillon, P. Cloud detection from a sequence of SST images. *Remote Sens. Environ.* **1996**, *55*, 80–88. [CrossRef]
67. Vázquez, D.P.; Atae-Allah, C.; Escamilla, P.L.L. Entropic approach to edge detection for SST images. *J. Atmos. Ocean. Technol.* **1999**, *16*, 970–979. [CrossRef]
68. Ullman, D.S.; Cornillon, P.C. Evaluation of front detection methods for satellite-derived SST data using in situ observations. *J. Atmos. Ocean. Technol.* **2000**, *17*, 1667–1675. [CrossRef]
69. Ullman, D.S.; Cornillon, P.C. Continental shelf surface thermal fronts in winter off the northeast US coast. *Cont. Shelf Res.* **2001**, *21*, 1139–1156. [CrossRef]
70. Belkin, I.M.; Cornillon, P.; Ullman, D. Ocean fronts around Alaska from satellite SST data. In Proceedings of the American Meteorological Society's 7th Conference on the Polar Meteorology and Oceanography and Joint Symposium on High-Latitude Climate Variations, Hyannis, MA, USA, 12–16 May 2003; Volume 12.
71. Belkin, I.; Cornillon, P. Surface thermal fronts of the Okhotsk Sea. *Pac. Oceanogr.* **2004**, *2*, 6–19.
72. Belkin, I.; Cornillon, P. Bering Sea thermal fronts from Pathfinder data: Seasonal and interannual variability. *Pac. Oceanogr.* **2005**, *3*, 6–20.
73. Belkin, I.; Shan, Z.; Cornillon, P. Global survey of oceanic fronts from Pathfinder SST and in-situ data. In: Abstracts of the AGU 1998 Fall Meeting. *Eos Trans. AGU* **1998**, *79* (Suppl. 45), F475.
74. Belkin, I.; Cornillon, P.; Shan, Z. Global survey of ocean fronts from Pathfinder SST data. In Proceedings of the Oceanography Society Meeting, Miami Beach, FL, USA, 2–5 April 2001; p. 10.
75. Belkin, I.M.; O'Reilly, J.E. An algorithm for oceanic front detection in chlorophyll and SST satellite imagery. *J. Mar. Syst.* **2009**, *78*, 319–326. [CrossRef]
76. Kahru, M.; Håkansson, B.; Rud, O. Distributions of the sea-surface temperature fronts in the Baltic Sea as derived from satellite imagery. *Cont. Shelf Res.* **1995**, *15*, 663–679. [CrossRef]
77. Mavor, T.P.; Bisagni, J.J. Seasonal variability of sea-surface temperature fronts on Georges Bank. *Deep Sea Res. Part II Top. Stud. Oceanogr.* **2001**, *48*, 215–243. [CrossRef]
78. Nieto, K.; Demarcq, H. Multi-image edge detection on SST and chlorophyll satellite images in northern Chile. In *Report of the Workshop on Indices of Mesoscale Structures (WKIMS)*; 2006; pp. 22–24.
79. Breaker, L.C.; Mavor, T.P.; Broenkow, W.W. *Mapping and Monitoring Large-Scale Ocean Fronts off the California Coast Using Imagery from the GOES-10 Geostationary Satellite*; The Regents of the University of California: Oakland, CA, USA, 2005.
80. Kostianoy, A.G.; Ginzburg, A.I.; Frankignoulle, M.; Delille, B. Fronts in the Southern Indian Ocean as inferred from satellite sea surface temperature data. *J. Mar. Syst.* **2004**, *45*, 55–73. [CrossRef]
81. Moore, J.K.; Abbott, M.R.; Richman, J.G. Variability in the location of the Antarctic Polar Front (90–20 W) from satellite sea surface temperature data. *J. Geophys. Res. Ocean.* **1997**, *102*, 27825–27833. [CrossRef]
82. Moore, J.K.; Abbott, M.R.; Richman, J.G. Location and dynamics of the Antarctic Polar Front from satellite sea surface temperature data. *J. Geophys. Res. Ocean.* **1999**, *104*, 3059–3073. [CrossRef]
83. Kazmin, A.S.; Rienecker, M.M. Variability and frontogenesis in the large-scale oceanic frontal zones. *J. Geophys. Res. Ocean.* **1996**, *101*, 907–921. [CrossRef]
84. Shimada, T.; Sakaida, F.; Kawamura, H.; Okumura, T. Application of an edge detection method to satellite images for distinguishing sea surface temperature fronts near the Japanese coast. *Remote Sens. Environ.* **2005**, *98*, 21–34. [CrossRef]
85. Castelao, R.M.; Mavor, T.P.; Barth, J.A.; Breaker, L.C. Sea surface temperature fronts in the California Current System from geostationary satellite observations. *J. Geophys. Res. Ocean.* **2006**, *111*. [CrossRef]
86. Civco, D.L. Artificial neural networks for land-cover classification and mapping. *Int. J. Geogr. Inf. Sci.* **1993**, *7*, 173–186. [CrossRef]
87. Erol, H.; Akdeniz, F. A new supervised classification method for quantitative analysis of remotely-sensed multi-spectral data. *Int. J. Remote Sens.* **1998**, *19*, 775–782. [CrossRef]
88. Flygare, A.M. A comparison of contextual classification methods using Landsat TM. *Int. J. Remote Sens.* **1997**, *18*, 3835–3842. [CrossRef]
89. Jenks, G.F. The data model concept in statistical mapping. *Int. Yearb. Cartogr.* **1967**, *7*, 186–190.
90. Goodchild, M.; Haining, R.; Wise, S. Integrating GIS and spatial data analysis: Problems and possibilities. *Int. J. Geogr. Inf. Syst.* **1992**, *6*, 407–423. [CrossRef]
91. Osaragi, T. *Classification Methods for Spatial Data Representation*; Centre for Advanced Spatial Analysis (UCL): London, UK, 2002.
92. Poulain, P.M. Adriatic Sea surface circulation as derived from drifter data between 1990 and 1999. *J. Mar. Syst.* **2001**, *29*, 3–32. [CrossRef]
93. Barkley, R. The Kuroshio current. *Sci. J.* **1970**, *6*, 54–60.
94. Macdonald, A.M.; Wunsch, C. An estimate of global ocean circulation and heat fluxes. *Nature* **1996**, *382*, 436–439. [CrossRef]
95. Nitani, H. Beginning of the Kuroshio. In *Kuroshio, Physical Aspect of the Japan Current*; University of Washington Press: Seattle, WA, USA, 1972.
96. Feng, M.; Mitsudera, H.; Yoshikawa, Y. Structure and variability of the Kuroshio Current in Tokara Strait. *J. Phys. Oceanogr.* **2000**, *30*, 2257–2276. [CrossRef]
97. Nakamura, H.; Ichikawa, H.; Nishina, A.; Lie, H.J. Kuroshio path meander between the continental slope and the Tokara Strait in the East China Sea. *J. Geophys. Res. Ocean.* **2003**, *108*. [CrossRef]

98. Nitani, H. On the phase velocity of the large meander of the Kuroshio off Kyushu and Enshu-Nada: Large meander of the Kuroshio in 1975–1980 (III) *Rep. Hydrogr. Res.*; **1982**, *17*, 229–239.
99. Andres, M.; Jan, S.; Sanford, T.B.; Mensah, V.; Centurioni, L.R.; Book, J.W. Mean structure and variability of the Kuroshio from northeastern Taiwan to southwestern Japan. *Oceanography* **2015**, *28*, 84–95. [CrossRef]
100. Rio, M.; Mulet, S.; Picot, N. New global Mean Dynamic Topography from a GOCE geoid model, altimeter measurements and oceanographic in-situ data. In Proceedings of the ESA living Planet Symposium, Edinburgh, UK, 9–13 September 2013.
101. Ubelmann, C.; Klein, P.; Fu, L.L. Dynamic interpolation of sea surface height and potential applications for future high-resolution altimetry mapping. *J. Atmos. Ocean. Technol.* **2015**, *32*, 177–184. [CrossRef]
102. Reynolds, R.W.; Rayner, N.A.; Smith, T.M.; Stokes, D.C.; Wang, W. An improved in situ and satellite SST analysis for climate. *J. Clim.* **2002**, *15*, 1609–1625. [CrossRef]
103. Reynolds, R.W.; Smith, T.M.; Liu, C.; Chelton, D.B.; Casey, K.S.; Schlax, M.G. Daily high-resolution-blended analyses for sea surface temperature. *J. Clim.* **2007**, *20*, 5473–5496. [CrossRef]
104. Huang, B.; Banzon, V.F.; Freeman, E.; Lawrimore, J.; Liu, W.; Peterson, T.C.; Smith, T.M.; Thorne, P.W.; Woodruff, S.D.; Zhang, H.M. Extended reconstructed sea surface temperature version 4 (ERSST. v4). Part I: Upgrades and intercomparisons. *J. Clim.* **2015**, *28*, 911–930. [CrossRef]
105. Huang, B.; L'Heureux, M.; Hu, Z.Z.; Zhang, H.M. Ranking the strongest ENSO events while incorporating SST uncertainty. *Geophys. Res. Lett.* **2016**, *43*, 9165–9172. [CrossRef]
106. Yu, L.; Weller, R.A. Objectively analyzed air–sea heat fluxes for the global ice-free oceans (1981–2005). *Bull. Am. Meteorol. Soc.* **2007**, *88*, 527–540. [CrossRef]
107. Yu, C.; Hu, D.; Wang, S.; Chen, S.; Wang, Y. Estimation of anthropogenic heat flux and its coupling analysis with urban building characteristics—A case study of typical cities in the Yangtze River Delta, China. *Sci. Total Environ.* **2021**, *774*, 145805. [CrossRef]
108. Song, X.; Yu, L. High-latitude contribution to global variability of air–sea sensible heat flux. *J. Clim.* **2012**, *25*, 3515–3531. [CrossRef]
109. Rousseaux, C.S.; Gregg, W.W. Recent decadal trends in global phytoplankton composition. *Glob. Biogeochem. Cycles* **2015**, *29*, 1674–1688. [CrossRef]
110. Ford, D.; Barciela, R. Global marine biogeochemical reanalyses assimilating two different sets of merged ocean colour products. *Remote Sens. Environ.* **2017**, *203*, 40–54. [CrossRef]
111. Platt, T.; Sathyendranath, S.; Forget, M.H.; White III, G.N.; Caverhill, C.; Bouman, H.; Devred, E.; Son, S. Operational estimation of primary production at large geographical scales. *Remote Sens. Environ.* **2008**, *112*, 3437–3448. [CrossRef]
112. Ciavatta, S.; Kay, S.; Saux-Picart, S.; Butenschön, M.; Allen, J. Decadal reanalysis of biogeochemical indicators and fluxes in the North West European shelf-sea ecosystem. *J. Geophys. Res. Ocean.* **2016**, *121*, 1824–1845. [CrossRef]
113. Sathyendranath, S.; Brewin, R.J.; Brockmann, C.; Brotas, V.; Calton, B.; Chuprin, A.; Cipollini, P.; Couto, A.B.; Dingle, J.; Doerffer, R.; et al. An ocean-colour time series for use in climate studies: The experience of the ocean-colour climate change initiative (OC-CCI). *Sensors* **2019**, *19*, 4285. [CrossRef]
114. Pujol, M.I.; Faugère, Y.; Taburet, G.; Dupuy, S.; Pelloquin, C.; Ablain, M.; Picot, N. DUACS DT2014: The new multi-mission altimeter data set reprocessed over 20 years. *Ocean. Sci.* **2016**, *12*, 1067–1090. [CrossRef]
115. SChmitt, R.W. Salinity and the global water cycle. *Oceanography* **2008**, *21*, 12–19. [CrossRef]
116. Frankignoul, C.; Deshayes, J.; Curry, R. The role of salinity in the decadal variability of the North Atlantic meridional overturning circulation. *Clim. Dyn.* **2009**, *33*, 777–793. [CrossRef]
117. Umbert, M.; Hoareau, N.; Turiel, A.; Ballabrera-Poy, J. New blending algorithm to synergize ocean variables: The case of SMOS sea surface salinity maps. *Remote Sens. Environ.* **2014**, *146*, 172–187. [CrossRef]
118. Droghei, R.; Nardelli, B.B.; Santoleri, R. Combining in situ and satellite observations to retrieve salinity and density at the ocean surface. *J. Atmos. Ocean. Technol.* **2016**, *33*, 1211–1223. [CrossRef]
119. Droghei, R.; Buongiorno Nardelli, B.; Santoleri, R. A new global sea surface salinity and density dataset from multivariate observations (1993–2016). *Front. Mar. Sci.* **2018**, *5*, 84. [CrossRef]
120. Athick, A.M.A.; Naqvi, H.R. A method for compositing MODIS images to remove cloud cover over Himalayas for snow cover mapping. In Proceedings of the 2016 IEEE International Geoscience and Remote Sensing Symposium (IGARSS), Beijing, China, 10–15 July 2016; pp. 4901–4904.
121. Mohammed, A.A.A.; Naqvi, H.R.; Firdouse, Z. An assessment and identification of avalanche hazard sites in Uri sector and its surroundings on Himalayan mountain. *J. Mt. Sci.* **2015**, *12*, 1499. [CrossRef]
122. Belkin, I.; Mikhailichenko, Y.G. Thermohaline Structure of the Frontal Zone of the Northwest Pacific-Ocean at 160°-E. *Okeanologiya* **1986**, *26*, 70–72.
123. Paris, S.; Hasinoff, S.W.; Kautz, J. Local Laplacian filters: Edge-aware image processing with a Laplacian pyramid. *ACM Trans. Graph.* **2011**, *30*, 68. [CrossRef]
124. Alcaras, E.; Parente, C.; Vallario, A. Automation of Pan-Sharpening Methods for Pléiades Images Using GIS Basic Functions. *Remote Sens.* **2021**, *13*, 1550. [CrossRef]
125. Al-Amri, S.S.; Kalyankar, N.; Khamitkar, S. Image segmentation by using edge detection. *Int. J. Comput. Sci. Eng.* **2010**, *2*, 804–807.

126. Senthilkumaran, N.; Rajesh, R. Image segmentation-a survey of soft computing approaches. In Proceedings of the 2009 International Conference on Advances in Recent Technologies in Communication and Computing, Kottayam, India, 27–28 October 2009; pp. 844–846.
127. Al-Amri, S.S.; Kalyankar, N.; Khamitkar, S. Contrast stretching enhancement in remote sensing image. *BIOINFO Sens. Netw.* **2011**, *1*, 6–9.
128. Mokhtar, N.; Harun, N.H.; Mashor, M.Y.; Mustafa, N.; Adollah, R.; Mohd Nasir, N.F. *Image Enhancement Techniques Using Local, Global, Bright, Dark and Partial Contrast Stretching for Acute Leukemia Images*; Perpustakaan Tuanku Syed Faizuddin Putra: Arau, Malaysia, 2009.
129. Köhl, M.; Lister, A.; Scott, C.T.; Baldauf, T.; Plugge, D. Implications of sampling design and sample size for national carbon accounting systems. *Carbon Balance Manag.* **2011**, *6*, 1–20. [CrossRef] [PubMed]
130. Wang, J.; Chen, A.; Yu, H. Sea Surface Temperature variations over Kuroshio in the East China Sea. *E3S Web Conf.* **2019**, *131*, 01048. [CrossRef]
131. Lacorata, G.; Corrado, R.; Falcini, F.; Santoleri, R. FSLE analysis and validation of Lagrangian simulations based on satellite-derived GlobCurrent velocity data. *Remote Sens. Environ.* **2019**, *221*, 136–143. [CrossRef]
132. He, Y.; Wang, X.; Li, D.; Xie, Z.; Chai, C. Typhoon disaster damage assessment and disaster situation web visu-alization based on NPP-VIIRS nighttime light remote sensing. In Proceedings of the AIIPCC 2021; The Second International Conference on Artificial Intelligence, Information Processing and Cloud Computing, Hangzhou, China, 26–28 June 2021; pp. 1–8.
133. Kawai, H.; Saitoh, S.i. Secondary fronts, warm tongues and warm streamers of the Kuroshio Extension system. *Deep. Sea Res. Part A Oceanogr. Res. Pap.* **1986**, *33*, 1487–1507. [CrossRef]
134. Guo, X.; Miyazawa, Y.; Yamagata, T. The Kuroshio onshore intrusion along the shelf break of the East China Sea: The origin of the Tsushima Warm Current. *J. Phys. Oceanogr.* **2006**, *36*, 2205–2231. [CrossRef]
135. Xue, H.; Chai, F.; Pettigrew, N.; Xu, D.; Shi, M.; Xu, J. Kuroshio intrusion and the circulation in the South China Sea. *J. Geophys. Res. Ocean.* **2004**, *109*. [CrossRef]
136. Donohue, K.A.; Watts, D.R.; Tracey, K.L.; Greene, A.D.; Kennelly, M. Mapping circulation in the Kuroshio Extension with an array of current and pressure recording inverted echo sounders. *J. Atmos. Ocean. Technol.* **2010**, *27*, 507–527. [CrossRef]
137. Mizuno, K.; White, W.B. Annual and interannual variability in the Kuroshio current system. *J. Phys. Oceanogr.* **1983**, *13*, 1847–1867. [CrossRef]
138. Belkin, I.; Cornillon, P. SST fronts of the Pacific coastal and marginal seas. *Pac. Oceanogr.* **2003**, *1*, 90–113.